PULSED LASERS IN LIDAR APPLICATION: MODELS FOR OPTIMIZING WIND TURBINE PERFORMANCE

A Thesis Presented to the Department of Theoretical and Applied Physics
African University of Science and Technology, Abuja
In partial fulfilment of the requirements for the award of

MASTER OF SCIENCE DEGREE

By

IROH MICHAEL CHIJIOKE

Supervised by

Dr. habil. Anatole Kenfack

African University of Science and Technology
www.aust.edu.ng
P.M.B 681, Garki, Abuja F.C.T
Nigeria.

June, 2019

PULSED LASERS IN LIDAR APPLICATION: MODELS FOR OPTIMIZING WIND TURBINE PERFORMANCE

By

IROH MICHAEL CHIJIOKE

A THESIS APPROVED BY THE DEPARTMENT OF THEORETICAL AND APPLIED PHYSICS

RECOMMENDED:

....

Supervisor: Dr. habil. Anatole Kenfack

....

Head, Department of Theoretical Physics

APPROVED:

....

Chief Academic Officer (Prof. C. E. Chidume)

....

Date

ABSTRACT

Since the appearance of the first wind turbines at the end of the nineteenth century, wind energy has been considered to be a renewable energy source for not just developed countries but also developing countries as well. Thus, since 2004, there has been a steady rise in wind energy production worldwide, with substantial actively installed capacity in Africa. However, due to the fact that wind turbines are highly dynamic systems that are excited by stochastic loads from the wind, variations in this disturbance usually medium-term (-*changes during the space of a few hours or minutes cause variations in power output which must be accepted by the system to which the turbine is connected*-) and short-term (*typically wind gusts which will introduce cyclic loadings which must be absorbed by the wind turbine with high susceptibility to fatigue damage*) negatively impacts heavily on Levelized Cost Of Energy (LCOE) of wind energy (*i.e., the average cost per unit of energy over the lifetime of the turbine, including capital costs, operations and maintenance costs, and all other relevant expenses*) [1].

As a result, there has been slow progress in the growth and development of more powerful turbines which have some significant advantages such as less visual impact to local people, and projects with more profitability. While traditional wind turbine control design utilize feedback control algorithms such as Artificial Neural Network (AAN) algorithms to address this challenge, this has often proved ineffective because they are only able to react to impacts of wind changes on the turbine dynamics after these impacts have already occurred [2].

Consequently, as a promising alternative, Light Detection and Ranging (Lidar) allows preview information about the approaching wind to be used to improve wind turbine control including blade pitch, generator torque, and yaw direction, thereby optimizing operational performance of the wind turbine through increase in energy yield, while keeping structural loads low [3]. Therefore, it is our goal in this thesis to carry out a thorough exposition of modeling associated with this trend. We will first focus on lidar system modeling with particular emphasis on the laser device which is the primary component of the lidar systems. Then we will explore wind and wind turbine modeling through aero-elastic simulations, and then wind field reconstructions with correlations between Lidar systems and Wind turbines [4]. We will end with an insight into what is to be expected with regards to the lidar scanning

pattern and consequently the entire lidar-wind turbine models and simulations when pulsed Lasers operating in the pico and/or femtosecond regime are used in the laser system as against the traditional nanoseconds pulsed lasers.

ACKNOWLEDGMENTS

"Now to Him who is able to do more than we can ask or imagine according to His power operative in the church be all glory now and forever" (Eph. 3:20–21). I sincerely thank God who grants us enablement to achieve whatever feat in life. Indeed, 'it is in him that we live and move and have our being' (Acts 17:28).

I sincerely thank God and acknowledge with great gratitude the immediate sponsors of the M.Sc. program I did in AUST, the African Development Bank (ADB) and Pan African Material Institute (PAMI) as well as all the funding collaborators of AUST who continue to provide scholarship to Africans to study in this great centre of excellence. May God bless you richly.

To the entire management of the African University of Science and Technology, I am immensely grateful. Special thanks to the Acting President, Prof. Charles Chidume, and the academic team of the university. I am sincerely grateful to the HOD of Theoretical and Applied Physics Department, Prof. habil. Anatole Kenfack, who also doubled as my project supervisor. Thanks prof. for your guidance and inspiration.

My gratitude goes to the immediate research team that worked assiduously to come up with these results. Special mention of Emmanuel Onwukwe, David Clement and Yerima Williams. To you Irewole Iyomo, you are simply indescribable. Thanks for the pains of always going back and forth with ideas and great commitment you manifested in this research. May God bless you abundantly.

I want to equally thank the entire 2019 M.Sc. group and in particular the smaller group of M.Sc. Physics 2019. Your encounter and friendship contributed in no small measure. Thanks so much.

I acknowledge and thank Rev. Sr. Chinyerem Onyekanne,IHM who by the way introduced me to AUST. You really became a mentor in every sense of the word. Thanks so much. Special thanks too to: Amaka, Paulina, Nsima, Daalu, Yvet, Cynthia, Obi, and Cyril. Thanks for your various levels of help in the course of the M.Sc. program.

I am immensely thankful to all the faculties and visiting professors who inspired us to work hard. You have made an indelible mark in me that further motivates me in terms of academic work. May God bless and reward you all.

I acknowledge and thank my Provincial Superior, Very Rev. Fr. Cyril N.

Mbata,CM for giving me the permission to undertake this studies. I acknowledge special encouragements from Frs. Damian Nwankwo,CM; Michael Ngoka,CM; Sixtus Njoku,CM; Evarestus Igwe,CM and indeed the confreres who are members of Abuja local community, past and present.

To several others I could not put down your names, be sure that you are highly acknowledged and appreciated. Wole also did the type setting; thanks for that extra labour too.

DEDICATION

This research work is dedicated to my beloved father, *Late chief Vincent Iroh Elum*, the man who taught me the beauty of resilience. I dedicate this work too to all Nigerians who are committed to the course of providing constant electricity to the 200 million citizens of this nation!

CONTENTS

LIST OF TABLES

LIST OF FIGURES

CHAPTER 1

INTRODUCTION

1.1 Background and Motivation

"The fuel in the earth will be exhausted in a thousand or more years, and its mineral wealth, but man will find substitutes for these in the winds, the waves, the sun's heat, and so forth." True to those words of *John Burroughs* uttered over a century ago, man is really finding viable renewable energy alternatives in the wind. In fact, since the appearance of the first wind turbines at the end of the nineteenth century, wind energy has been considered to be a renewable energy source for not just developed countries but also developing countries as well. Thus, there has been a steady rise in wind energy production worldwide since 2004, with substantial actively installed capacity in Africa. In fact, in [5], it was noted that wind energy is the "fastest growing installed alternative-energy production", with at least 20% of United States energy expected to be supplied by offshore and onshore wind farms by 2030.

Renewable energies constitute excellent solutions to both the increase of energy consumption and environment problems. Among these energies, wind energy is very interesting. Wind energy is the subject of advanced research. In the development of wind turbine, the design of its different structures is very important. It will ensure: the robustness of the system, the energy efficiency, the optimal cost and the high reliability. The use of advanced control technology and new technology products allows bringing the wind energy conversion system in its optimal operating mode. Different strategies of control can be applied on generators, systems relating to blades, etc. in order to extract maximal power from the wind [6].

To achieve this ambitious goal, the cost of wind energy must be able to compete favorably with the cost of traditional fossil fuels. This implies that the *Levelized Cost Of Energy (LCOE)* of wind energy defined as the average cost per unit of energy over the lifetime of the wind turbine, including capital costs, operations and maintenance costs, and all other relevant expenses [3], usually expressed in \$/kWh, must be significantly reduced. A typical conventional approach to this will be to increase wind energy production, and so the trend within the last three decades has been the development and deployment of larger and more powerful wind turbines. As at 2017, according to [7], Vestas V-164 rated at 9.5 MW is the most powerful wind turbine. The rationale behind this, no doubt is primarily to harness more wind resources and increase profitability, though some secondary reasons such as aesthetics, less visual impact to local people and environmental issues cannot be neglected. This approach in itself has not been without daunting challenges. To understand these challenges, consider briefly the design and operation of a wind turbine.

A cutaway-section of the dominant horizontal axis three-blade wind turbine is shown in figure 1.1 below:

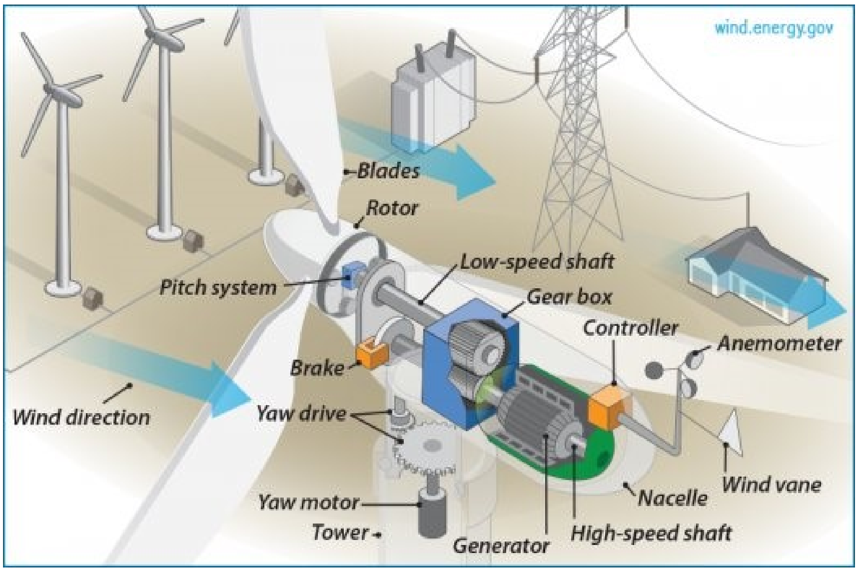

Figure 1.1: A cut-away section of a horizontal axis three-blade wind turbine

From the diagram above, the turbine consists of three main parts namely the blades, the nacelle and the tower. The blades which are fastened to the nacelle by means of the rotor are subjected to rotational motion by the wind. This rotational motion is amplified by the gearbox, high speed and low speed shafts in the nacelle which then rotates the generator (which is also in the nacelle), and the generator in turn produces Direct Current. The whole structure is supported by the tower. This simple but powerful picture underscores the fact that wind turbines are highly dynamic systems that are excited by stochastic loads from the wind. These winds are generally not predictable or dependable as variations in this disturbance often occur. These variations can be medium-term that is changed during the space of a few hours or minutes cause variations in power output which must be accepted by the system to which the turbine is connected, or short-term – typically wind gusts which will introduce cyclic loadings which must be absorbed by the wind turbine with high susceptibility to fatigue damage. As shown above, these variations are managed by control systems on the nacelle such as the pitch system for the blades and the brake for generator control, as well as the yaw motor fitted in the tower. Sadly, these controls rely on traditional feedback mechanism based on algorithms such as Artificial Neural Network (AAN) algorithms, which are only able to react to impacts of wind changes on the turbine dynamics after these impacts have already occurred, thereby impacting negatively on LCOE. The situation is best illustrated with an individual riding a bicycle with a blind fold, who only reacts when he/she must have crashed into something or had an impact.

Given this scenario, a natural question follows: What if the individual could ride the bicycle with his eyes open, thereby seeing the obstacle before hand and consequently avoiding the impact or crash? Hence, as a promising alternative, Light Detection and Ranging (Lidar) allows preview information about the approaching wind to be used to improve wind turbine control including blade pitch, generator torque, and yaw direction, thereby optimizing operational performance of the wind turbine through increase in energy yield, while keeping structural loads low [1].

1.2 The Problem

As stated clearly in the abstract as well as in the analysis of a typical wind turbine parts in the introduction above, the problem that light detecting and ranging devices hope to address, at least theoretically in the models and in systems that has begun to implement same is the erratic behavior of the approaching wind in front of the turbine and the feedback method of collecting data for optimization by the traditional models. As Eric Simley, Holger Fürst, Florian Haizmann and David Schlipf, in the article "Optimizing Lidars for Wind Turbine Control Applications–Results from the IEA Wind Task 32 Workshop" *Remote Sens.* **2018**, *10, 863* noted clearly, these approach has proved to be ineffective in addressing the problem of control and design in the wind energy development. In their very words, due to the fact that wind turbines are highly dynamic systems that are excited by stochastic loads from the wind, variations in this disturbance usually medium-term (-*changes during the space of a few hours or minutes cause variations in power output which must be* *accepted by the system to which the turbine is connected*-) and short-term (*typically wind gusts which will introduce cyclic loadings which must be absorbed by the wind turbine with high susceptibility to fatigue damage*) negatively impacts heavily on Levelized Cost Of Energy (LCOE) of wind energy (*i.e., the average cost per unit of energy over the lifetime of the turbine, including capital costs, operations and maintenance costs, and all other relevant expenses*) [1]. As a result, there has been slow progress in the growth and development of more powerful turbines which have some significant advantages such as less visual impact to local people, and projects with more profitability. While traditional wind turbine control design utilize feedback control algorithms such as Artificial Neural Network (AAN) algorithms to address this challenge, this has often proved ineffective because they are only able to react to impacts of wind changes on the turbine dynamics after these impacts have already occurred [2]. Consequently, as a promising alternative, Light Detection and Ranging (Lidar) allows preview information about the approaching wind to be used to improve wind turbine control including blade pitch, generator torque, and yaw direction, thereby optimizing operational performance of the wind turbine through increase in energy yield, while keeping structural loads low [1].

1.3 The Aim

The general purpose or the overall goal of this research is to carry out an exhaustive exposition of modeling associated with the Lidar systems as it applies to wind turbines particularly with the pulsed laser systems as its main components. As seen from the literature review in chapter two, this is not a novel area for environments where wind turbine technology is already a household term. It is one of those technological applications aimed at improving the performance of the wind turbine over time.

1.4 Objectives

To achieve the set goal/aim of this research work, we shall employ the methodology outlined in the third chapter of the project. Consequently, we shall therefore approach the discussions on Lidar systems as it applies to wind turbine technology by laying the physical foundations upon which the technology rests. We will traditionally start as expected, the classical mechanics approach by seeing the turbine as a rigid body in motion. This will entail an analysis of the structural mechanics and the cyclic loading of wind turbines.

Another physical approach to the analysis of the wind turbine is the fluid mechanical approach. In this regard, we shall go back to the model established by Navier-stokes equation for compressible Newtonian flow and the aero-elastic simulation. In the main, the approaching wind before a turbine is essentially a compressible fluid hence the application of the relevant Navier-stokes equations. As is typical of the foundational mechanics of any physical systems, the discussions of the wind energy will obviously be incomplete without a quantum mechanical approach. The physics of the laser technology which is an essential part of the Lidar system is only clarified by the basic principles of quantum mechanics. The dynamic equation we shall employ here is the time dependent Schrodinger wave equation. The TDSE will enable us to elucidate the principles, the major components of the pulsed lasers operating at the nanoseconds regime for lidar systems. This will help to establish the correlation models and algorithms for the field reconstruction in view of formulating new insights into the laser scan patterns in the picoseconds and the femtoseconds regime.

Thus, we will explore wind and wind turbine modeling through aero-elastic simulations, and then wind field reconstructions with correlations between Lidar systems and Wind turbines [4]. We will end with an insight into what is to be expected with regards to the lidar scanning pattern and consequently the entire lidar-wind turbine models and simulations when pulsed Lasers operating in the pico and/or femtosecond regime are used in the laser system as against the traditional nanoseconds pulsed lasers.

1.5 Significance

This thesis is expected to significantly contribute to the theoretical understanding of the correlation between wind turbines and lidar systems by providing invaluable insights into overcoming the barriers preventing the widespread use of Lidars for wind turbine control strategies for overcoming those barriers, and ideas for maximizing the effectiveness of Lidars for control applications. The significance of this research follows the main purpose of the International Energy Agency (IEA) wind task workshop 32 that was held in Boston, MA, USA in July 2016 [8]. Thus, the significance of this research follows the analysis of Eric Simley et al [1] who argued that: The workshop, ‘optimising Lidar designs for wind energy applications’ was held to identify Lidar system properties that are desirable for wind turbine control applications and help foster the widespread application of Lidar-assisted control (LAC).

Through multidisciplinary approach which is the modern trend of LAC, researches of this type will join the myriads of standard literatures in Journals to further overcome the barriers to the use of Lidar for wind turbine control such as optimization of lidar scan patterns by minimizing the error between the measurement and rotor effective wind speed. In addition, frequency domain methods for directly calculating measurement error using a stochastic wind field model. This process is applied to the optimization of several continuous waves and pulsed Doppler Lidar scan patterns. Also, the research intends to contribute to the design process for a Lidar-assisted pitch controller for rotor speed regulation. Again, using measurements from an optimized scan pattern shows that the rotor speed regulation obtained after optimizing the LAC scenario through time domain simulations matches the performance predicted by the theoretical frequency domain model [9].

1.6 Scope of Work

We will first focus on lidar system modeling with particular emphasis on the laser device which is the primary component of the lidar systems. Then we will explore wind and wind turbine modeling through aero-elastic simulations, and then wind field reconstructions with correlations between Lidar systems and Wind turbines [4].

Many of the literature in the Lidar applications to wind turbine technology as we shall see in chapter three focus on the results of the scan pattern of the pulsed lasers in the nanoseconds regime. Consequently, in the spirit of experimental extrapolation, we shall attempt theoretically and in the python codes to simulate lidar systems for Pico and Femto seconds pulsed lasers. We will end with an insight into what is to be expected with regards to the lidar scanning pattern and consequently the entire lidar-wind turbine models and simulations when pulsed Lasers operating in the pico and/or femtosecond regime are used in the laser system as against the traditional nanoseconds pulsed lasers.

1.7 Limitation of Work

This work will focus on three-bladed horizontal axis wind turbines operating in average wind speed areas. We will not attempt to consider other types of wind turbines neither will we attempt to consider wind turbines operating in low wind speed areas.

The available time and space are the necessary conditions that compel this limitation to the research work. To achieve results that are essentially measurable and susceptible to scientific tests using modern data analysis means, it is necessary to focus only on a particular aspect of the wind technology while leaving a huge corpus to further research and development. This is the trend we hope to approach the research work as it will be evident in the subsequent chapters of the work.

CHAPTER 2

LITERATURE REVIEW

The essence of this chapter is to illustrate the growth in literature theories on the optimization of wind turbine performance using pulsed lasers in LIDAR applications. In this regard therefore, this chapter has been broken down into conceptual framework, theoretical and empirical literatures that are relevant to the topic under study. The main concepts reviewed here are; wind turbines and wind modeling (where we discuss the physics, technology and aero-elastic simulations of wind turbines and modeling); LIDAR and LIDAR modeling; and the correlation between wind systems and LIDAR systems.

2.1 Wind Turbines and Wind Modeling

Over the past few years, there have been an increase in the production of energy by wind turbines, because its production is environmentally safe and friendly; therefore, the technology developed for the production of energy through wind turbines is accompanied by great challenges in the investigation [10]. The wind does not only serve as an energy source for wind turbines but also as the most important stochastic disturbance to the wind turbine control system. Thus, information about the wind inflow is valuable to optimize the energy production and reduce the structural loads [11].

2.1.1 The Physics of Wind Energy

What is Wind?

Wind is the flow of gases on a very large scale. Winds are generally caused by uneven heating of the atmosphere by the sun, the irregularities of the earth's surface, and the rotation of the earth. However, wind flow patterns are modified by the earth's terrain features, bodies of water, and surrounding vegetation. The sun does not heat up the earth's atmosphere evenly, as most of the solar energy is absorbed at the equator. When the air becomes heated it expands creating an area of higher pressure. Diffusion causes this area of higher pressure to move to an area of lower pressure. On a very large scale this would cause massive amounts of air to travel from one area to another, creating vast amounts of kinetic energy that can be harnessed by humans through the use of wind turbine.

The Physics of a Wind Turbine

A wind turbine is used to harness the kinetic energy of vast amounts of wind, and transform it into electricity. This can be shown with a very simple calculation. First we need to remember that wind is an air mass moving from an area of high pressure to an area of low pressure. This movement of air is kinetic energy which for an air mass m moving at a velocity v can be expressed as:

$$E_k = \frac{1}{2}mv^2 \tag{2.1}$$

Considering a certain cross-sectional area A, through which the air passes at velocity v, the volume $\dot{V}$ flowing through during a certain time unit, the so-called volume flow, is:

$$\dot{V} = vA \tag{2.2}$$

And the mass flow with air density ρ is:

$$\dot{m} = \rho v A \tag{2.3}$$

This mass flow can now be substituted into the formula for kinetic energy of the moving air to give the amount of energy passing through cross-section A per unit time. This energy is physically identical to the power P:

$$P = \frac{1}{2}\rho v^3 A \tag{2.4}$$

Therefore the amount of energy in the wind is controlled by the density, surface area and velocity of the moving air. This equation shows that selecting an area of high wind velocity is the most crucial part of picking out an area to place a wind turbine.

In reality, the equation for kinetic energy of wind does not represent the amount of energy that a wind turbine is able to harness. Wind turbines are not 100% efficient, and are unable to convert all of the kinetic energy into wind. If a wind turbine was 100% efficient then wind speeds would drop to 0 km/h after passing through the turbine. Albert Betz published a book in 1926 that showed it is only possible to extract 16/27 or 59% of the energy from a wind turbine. This is called Betz's law [12]. Therefore the theoretical energy model for a wind turbine is:

$$P = \frac{16}{27} \cdot \frac{1}{2} \rho v^3 A \tag{2.5}$$

To prove Betz's law, we start by asking how much mechanical energy can be extracted from the free-stream airflow by an energy converter. As mechanical energy can only be extracted at the cost of the kinetic energy contained in the wind stream, this means that, with an unchanged mass flow, the flow velocity behind the wind energy converter decrease. Reduced velocity, however, means at the same time a widening of the cross-section, as the same mass flow must pass through it. It is thus necessary to consider the conditions in front of and behind the converter (see figure 2.1).

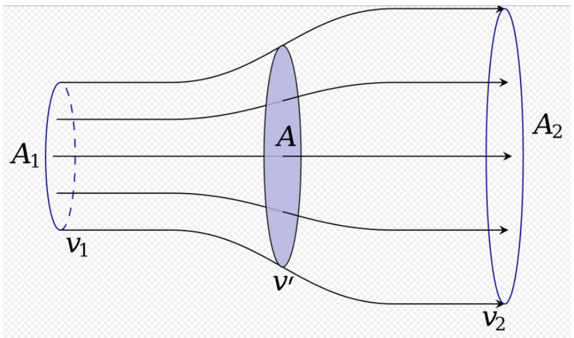

Figure 2.1: Flow conditions due to the extraction of mechanical energy from a free-stream air flow, according to the elementary momentum theory.

From the lettering in the diagram, v_1 is the un-delayed free-stream velocity, before it reaches the converter, whereas v_2 is the flow velocity behind the converter. The mechanical energy which the dis-shaped converter extracts from the airflow corresponds to the power difference of the air stream before and after the converter:

$$P = \frac{1}{2} \rho v_1^3 A_1 - \frac{1}{2} \rho v_2^3 A_2 = \frac{1}{2} \rho (v_1^3 A_1 - v_2^3 A_2) \tag{2.6}$$

The conservation of mass (continuity equation) requires that:

$$\rho v_1 A_1 = \rho v_2 A_2 \tag{2.7}$$

Thus,

$$P = \frac{1}{2} \rho v_1 A_1 (v_1^2 - v_2^2) \tag{2.8}$$

Or

$$P = \frac{1}{2}\dot{m}(v_1^2 - v_2^2) \tag{2.9}$$

From this equation it follows that, in purely formal terms, power would have to be at its maximum when v_2 is zero, namely when air is brought to a complete standstill by the converter. However, this result does not make sense physically. If the outflow velocity v_2 behind the converter is zero, then the inflow velocity before the converter must also become zero (from the continuity equation), implying that there would be no more flow through the converter at all. As could be expected, a physically meaningful result consists in a certain numerical ratio of v_2/v_1 where the extractable power reaches its maximum.

This requires another equation expressing the mechanical power of the converter. Using the law of conservation of momentum, the force which the air exerts on the converter can be expressed as:

$$F = \dot{m}(v_1 - v_2) \tag{2.10}$$

According to Newton's third law, this force, the thrust, must be counteracted by an equal force exerted by the converter on the airflow. The thrust, so to speak, pushes the air mass at air velocity v', present in the plane of flow of the converter. The power required for this is:

$$P = Fv' = \dot{m}(v_1 - v_2)v' \tag{2.11}$$

Thus, the mechanical power extracted from the air flow can be derived from the energy or power difference before and after the converter, on the one hand, and, on the other hand, from the thrust and the flow velocity. Equating these two expressions yields the relationship for the flow velocity v':

$$\frac{1}{2}\dot{m}(v_1^2 - v_2^2) = \dot{m}(v_1 - v_2)v' \tag{2.12}$$

Thus the flow velocity through the converter is equal to the arithmetic mean of v_1 and v_2:

$$v' = \frac{v_1 + v_2}{2} \tag{2.13}$$

The mass flow thus becomes:

$$\dot{m} = \rho A v' = \frac{1}{2}\rho A(v_1 + v_2) \tag{2.14}$$

And the mechanical power output of the converter can then be expressed as:

$$P = \frac{1}{4}\rho A(v_1^2 - v_2^2)(v_1 + v_2) \tag{2.15}$$

Comparing this power output with $P_0 = 1/2\rho v_1^3 A$ where P_0 provides a reference for P and is the power of the free-air stream which flows through the same cross-sectional area A, without mechanical power being extracted from it.

Now we define the "power coefficient" c_p as the ratio of the mechanical power extracted by the converter and that of the undisturbed air stream:

$$c_p = \frac{P}{P_0} = \frac{\frac{1}{4}\rho A(v_1^2 - v_2^2)(v_1 + v_2)}{\frac{1}{2}\rho v_1^3 A} \tag{2.16}$$

After some re-arrangement, the power coefficient can be specified directly as a function of the velocity ratio v_2/v_1:

$$c_p = \frac{P}{P_0} = \frac{1}{2}\left|1 - \left(\frac{v_2}{v_1}\right)^2\right|\left|1 + \frac{v_2}{v_1}\right| \tag{2.17}$$

The power coefficient now only depends on the ratio of air velocities before and after the converter. If this interrelationship is plotted graphically as shown in figure 2.2, or solved analytically, it can be seen that the power coefficient reaches a maximum at a velocity ratio of about 1/3.

With $v_2/v_1 = 1/3$, the maximum "ideal power coefficient" c_p becomes

$$c_p = \frac{16}{27} = 0.59 \tag{2.18}$$

This theoretical maximum for an ideal wind turbine is known as the Betz limit.

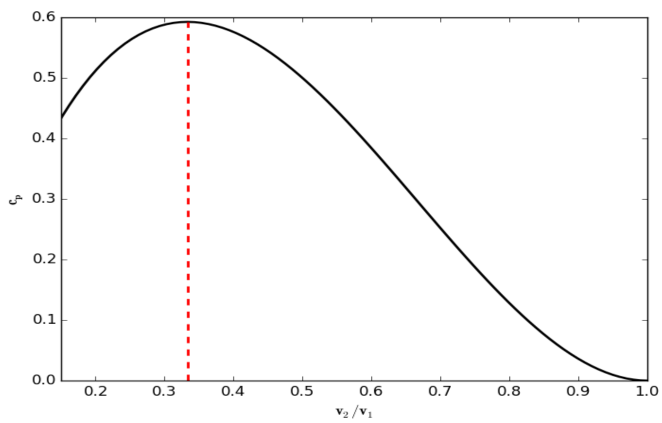

Figure 2.2: The power coefficient as a function of the velocity ratio for an ideal wind turbine.

Knowing that the maximum, ideal power coefficient is reached at $v_2/v_1 = 1/3$, the required velocity v_2 behind the converter can be calculated as:

$$v_2 = \frac{1}{2}v_1 \tag{2.19}$$

and the flow velocity v' is:

$$v' = \frac{2}{3}v_1 \tag{2.20}$$

The essential findings derived from Betz's law can be summarized in words as follows:

- The mechanical power which can be extracted from a free-stream airflow by an energy converter increases with the third power of the wind velocity.
- The power increases linearly with the cross-sectional area of the converter traversed; it thus increases with the square of its diameter.
- Even with an ideal airflow and lossless conversion, the ratio of extractable mechanical work to the power contained in the wind is limited to a value of 0.593. Hence, only about 59% of the wind energy of a certain cross-section can be converted into mechanical power.
- When the ideal power coefficient achieves its maximum value $c_p = 0.593$, the wind velocity in the plane of flow of the converter amounts to two thirds of the undisturbed wind velocity and is reduced to one third behind the converter.

2.1.2 What is a Wind Turbine?

The concept of harnessing wind energy to generate mechanical power goes back for millennia. As early as 5000 B.C., Egyptians used wind energy to propel boats along the Nile River. American colonists relied on windmills to grind grain, pump water and cut wood at sawmills. Today's wind turbines are the windmill's modern equivalent – converting the kinetic energy in wind into clean, renewable electricity.

How Does A Wind Turbine Work?

The operation is based on the scientific theory of fluid mechanics and some elements of aerodynamics. Modern wind turbines catch the wind by turning into or away from air flows. Wind moves the propeller mounted on a rotor and the movement turns a high-speed shaft coupled to an electric or induction generator.

The majority of wind turbines consist of three blades mounted to a tower made from tubular steel. There are less common varieties with two blades, or with concrete or steel lattice towers. At 100 feet or more above the ground, the tower allows the turbine to take advantage of faster speeds found at higher altitudes.

Turbines catch the wind's energy with their propeller-like blades, which act much like an airplane wing. When the wind blows, a pocket of low-pressure air forms on one side of the blade. The low-pressure air pocket the pulls the blade toward it, causing the rotor to turn. This is called lift. The force of the lift is much stronger than the wind's force against the front side of the blade, which is called drag. The combination of lift and drag causes the rotor to spin like propeller.

A series of gears increase the rotation of the rotor from about 18 revolutions per minute to about 1800 revolutions per minute – a speed that allows the turbine's generator to produce AC electricity. The major components of a wind turbine include a low-speed rotor consisting of two or three light-weight blades with optimum airfoil shapes operating at 30 to 60 rpm, a high-speed shaft mechanically coupled to low-speed via a gear box assembly and operating between 100 and 200 rpm, a pitch motor drive assembly, a yaw motor drive assembly, a nacelle, a wind vane indicator, an AC induction generator operating at a high speed, a speed controller unit, a tower structure, an anemometer, and other accessories necessary to provide mechanical integrity under heavy wind gusts. A step-up transformer at the base of the tower allows transfer of the wind-generated electricity to the utility power grid. All elements except the step-up transformer are located at the top of the tower as shown in the figure 2.3. The enclosure depicted in the figure rotates to enable the rotor blades to face into or away from the wind. This is essentially the working principle of a wind turbine. The wind moves the propeller that turns the low-speed and high-speed shafts. The high-speed shaft is connected to a generator capable of producing electrical energy.

The anemometer is a critical element of a wind turbine. It gauges wind speed and direction and sends the information to the controller that in turn provides necessary data to critical elements of the system. The controller essentially directs the yaw motor to turn the rotor to face toward or away from the wind, depending on the wind direction. The gear box, the heaviest element of the system, converts the slow rotation (revolutions per minute or rpm) of the low-speed rotor shaft to higher rpm of the high-speed shaft which is mechanically coupled to a generator that produces the electricity. In brief, the high-speed shaft drives a generator that converts mechanical energy into electrical energy.

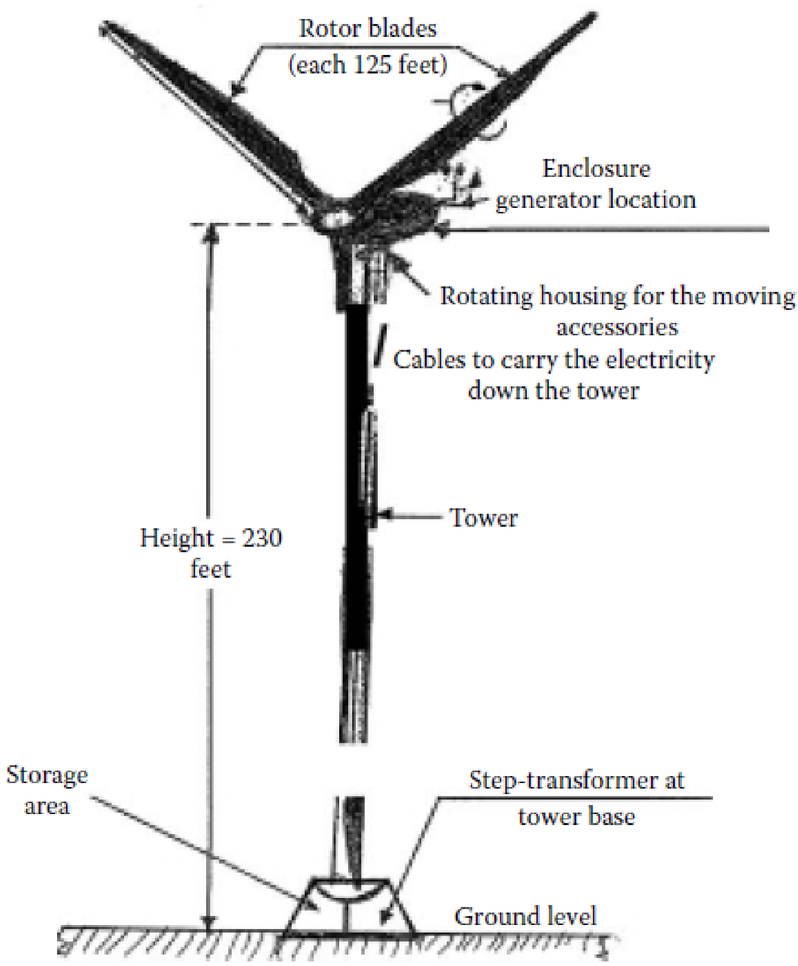

Figure 2.3: Wind turbine components.

Types of Wind Turbine

Wind turbines are classified into two major categories: horizontal axis wind turbines (HAWTs) and vertical axis wind turbines (VAWTs). Vertical axis turbines have a vertical shaft that is driven by blades that move horizontally like a roundabout. Horizontal axis describes the more conventional windmill which has to face itself into the wind and whose blades revolve in a vertical plane. The vertical axis wind turbine is popular even though it is thousands of years old and has long ago been superseded by technically by the horizontal axis blade rotor.

The HAWT category are widely used for commercial applications. A horizontal axis wind turbine may be of rotor-upwind design to face the wind or rotor-downward design to enable the wind pass the tower and nacelle before it hits the rotor. The tower height for HAWTs is extremely important because wind speed increases with the height above the ground. Rotor diameter is equally important because it determines the area needed to meet specific power output level.

The power output performance of a HAWT can be optimized by selecting a ratio between the rotor diameter (D) and the hub height (H) very close to unity. The rated power output of a wind turbine is the maximum power allowed for the installed electrical generator. The control system must ensure that this power is not exceeded in high-wind environments to avoid structural damage to the system. HAWT systems typically deploy two or three rotor blades. A turbine with two rotor blades is cheaper, but it rotates faster, thereby producing a visual flickering effect; also the aerodynamic efficiency of a two-blade rotor is lower than that of a three-blade rotor.

Attractive feature of the VAWT include the ability to take wind from any direction, and the ability to drive a generator at ground level. It has the advantage that the generator and the gear box be installed at the base of the tower, thereby making these components easy to service and repair. But in spite of a huge amount of research, vertical axis wind turbines have failed to become widely successful. They can be hard to start, hard to stop, and they have inherently lower efficiency than horizontal axis turbines. (They convert less of the energy that is in the wind). Both the Savonius and Darrieus turbines fall into this category and are available commercially. However, these turbines have small output capacities and hence are used for low-power applications such as battery charging in areas where power grids are not available.

2.1.3 Wind Modeling

Wind can be mathematically described by a set of three-dimensional wind speed vectors at each point in time and space. For aero-elastic simulations, the wind speed vectors are usually only generated at the rotor plane to calculate the aerodynamic forces and moments. In this thesis, a wind field over the full space in front of the turbine is necessary to simulate lidar systems, see figure 2.4.

In this section, we introduce the coordinate systems used in this thesis and describe the wind models for the lidar simulations and a reduced model for wind filed reconstruction.

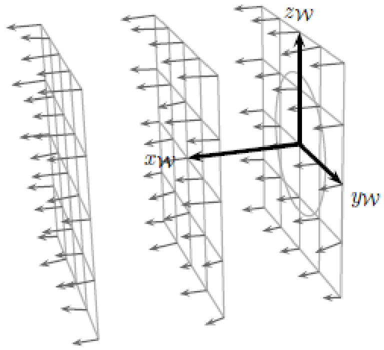

Figure 2.4: Snapshot of the time variant vector field as a general description of wind.

Wind and Inertial Coordinate System

The wind coordinate system is denoted in this work by the subscript $\mathcal{W}$. It is used to describe the wind flow and is aligned with the mean wind direction regarding the inertial coordinate system, which is denoted here by the subscript $\mathcal{I}$. The direction is defined by the horizontal inflow angle α_h (azimuth or rotation around the $z_\mathcal{I}$-axis) and the vertical inflow angle α_v (elevation or rotation around the rotated $y_\mathcal{I}$-axis), see figure 2.5. Although all six DOFs could be used in principle, a rotation of around the $x_\mathcal{I}$ is not considered in this work but might be useful for very complex terrain.

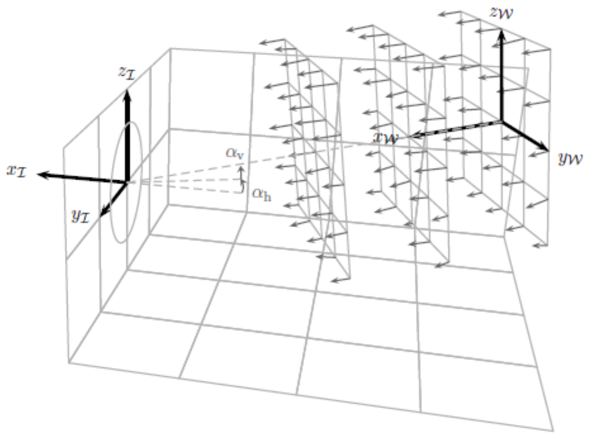

Figure 2.5: Orientation of the wind coordinate system (subscript $\mathcal{W}$) in the inertial coordinate system (subscript $\mathcal{I}$). Rotation order is defined as azimuth → elevation ($\alpha_h \rightarrow \alpha_v$).

The origin of the $\mathcal{W}$-system can be set according to the application. For lidar-assisted control, the origin of the $\mathcal{I}$ and the $\mathcal{W}$-system are usually located at the hub of the wind turbine. For ground based lidar systems, a translation to the measurement height can be useful.

If the origins of the $\mathcal{I}$ and the $\mathcal{W}$-system coincide, the transformation of the three wind speed components $[u_{i,\mathcal{W}} \quad v_{i,\mathcal{W}} \quad w_{i,\mathcal{W}}]^T$ in a point i from the wind to the inertial coordinate system is then calculated with the rotation matrix $\mathbf{T}_{\mathcal{I}\mathcal{W}}$ by

$$\begin{bmatrix} u_{i,\mathcal{I}} \\ v_{i,\mathcal{I}} \\ w_{i,\mathcal{I}} \end{bmatrix} = \underbrace{\underbrace{\begin{bmatrix} \cos(\alpha_h) & -\sin(\alpha_h) & 0 \\ \sin(\alpha_h) & \cos(\alpha_h) & 0 \\ 0 & 0 & 1 \end{bmatrix}}_{T_{\text{azimuth}}} \underbrace{\begin{bmatrix} \cos(\alpha_v) & 0 & \sin(\alpha_h) \\ 0 & 1 & 0 \\ -\sin(\alpha_v) & 0 & \cos(\alpha_v) \end{bmatrix}}_{T_{\text{elevation}}}}_{\mathbf{T}_{\mathcal{I}\mathcal{W}}} \begin{bmatrix} u_{i,\mathcal{W}} \\ v_{i,\mathcal{W}} \\ w_{i,\mathcal{W}} \end{bmatrix} \tag{2.21}$$

The transformation from the inertial to the wind coordinate system is done by

$$\begin{bmatrix} u_{i,\mathcal{W}} \\ v_{i,\mathcal{W}} \\ w_{i,\mathcal{W}} \end{bmatrix} = \mathbf{T}_{\mathcal{W}\mathcal{I}} \begin{bmatrix} u_{i,\mathcal{I}} \\ v_{i,\mathcal{I}} \\ w_{i,\mathcal{I}} \end{bmatrix} \quad \text{with} \quad \mathbf{T}_{\mathcal{W}\mathcal{I}} = \mathbf{T}_{\mathcal{I}\mathcal{W}}^{-1} = T_{\text{elevation}}^{-1} T_{\text{azimuth}}^{-1} \tag{2.22}$$

In most of this work, the wind turbine is assumed to be perfectly aligned with the mean wind direction. This implies that both inflow angles are zero and the wind coordinate system coincides with the inertial coordinate system.

2.2 LIDAR and Lidar Modeling

Lidar (LIght Detection And Ranging) is a remote sensing technology similar to radar (Radio Detection And Ranging) or sonar (SOund Navigation And Ranging). In the case of lidar, a light pulse is emitted into the atmosphere. Light from the beam is scattered in all directions from molecules and particulates in the atmosphere. A portion of the light is scattered back towards the lidar system. This light is collected by a telescope and focused upon a photodetector that measures the amount of backscattered light as a function of distance. The lidar system uses light in the form of a pulsed laser for powerful data collection that provides 3-D information for an area of interest. Among many things, it is useful for such tasks as surface mapping, vegetation mapping, transportation corridor mapping, transmission route mapping, and 3-D building mapping.

Over the last decades, lidar has largely contributed to our knowledge of our atmosphere. The interactions of the emitted light with the molecules and aerosols allow the observation of atmospheric parameters such as temperature, pressure, wind, humidity, and concentration of gases (ozone, methane, nitrous oxide, etc.) [14].

Lidar originated in the early 1960's, shortly after the invention of the laser. Its first applications came in meteorology where it was used to measure clouds [15]. Since then, lidar has been used not only in meteorology, but also in a wide range of other applications, such as laser range finders, altimeters, and satellite trackers [16].

The essential concept of lidar was originated by E. H Synge in 1930, who envisaged the use of powerful searchlights to probe the atmosphere [17, 18]. Indeed, lidar has since been used extensively for atmospheric research and meteorology. Lidar instruments fitted to aircraft and satellites carry out surveying and mapping – a recent example being the U.S. Geological Survey Experimental Advance Airbone Research Lidar [19]. NASA has identified lidar as a key technology for enabling autonomous precision safe landing of future robotic and crewed lunar-landing vehicles [20].

2.2.1 Lidar Operating Principle

The operating principle here is based on the assumption that wind speed has the same value as the small particles in the air, called aerosols. Pollen, droplets, smoke, and particles of dust form these particles. Lidar technology relies on detecting backscattered light from moving aerosols in the atmosphere, when illuminated by laser radiation with coherent detection (best for measuring Doppler shifts, or changes in phase of the reflected light). Coherent systems generally use optical heterodyne detection [21]. This is more sensitive than direct detection and allows them to operate at much lower power, but requires more complex transceivers. By measuring the Doppler frequency shift of the backscattered light, the wind speed can be determined remotely. The basic concept can be illustrated as in figure 2.6.

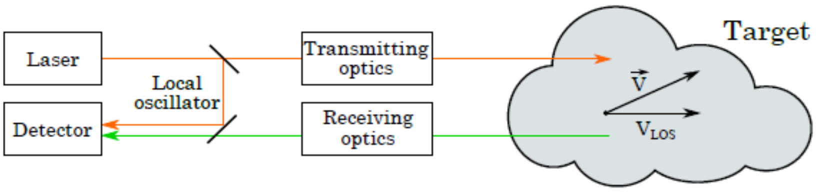

Figure 2.6: Generic Doppler lidar concept where **V** is the mean velocity of the target, and V_{los} is projected radial wind speed.

The radial speed component of the target, V_{los} (velocity measured along the line-of-sight) can be determined from the Doppler shift of the backscattered light using the expression

$$V_{\text{los}} = \frac{cf_D}{2f_L} = \frac{\lambda_L f_D}{2} \tag{2.23}$$

Where f_D is the Doppler shift c is the speed of light and λ_L the laser wavelength, which is typically in the order of 1.55 μm. Thus single lidar systems are only able to provide one-dimensional wind speed measurements.

2.2.2 Lidar Components

Lidar systems consist of several major components. See the figure 2.7 for a schematic representation of the major components of a lidar system. A lidar system consists of the following basic functional blocks: (1) a laser source of short, intense light pulses, (2) a photoreceiver, which collects the backscattered light and converts it into electrical signal, and (3) a computer/recording system, which digitizes the electrical signal as a function of time (or, equivalently, as a function of the range from the light source) as well as controlling the other basic functions of the system.

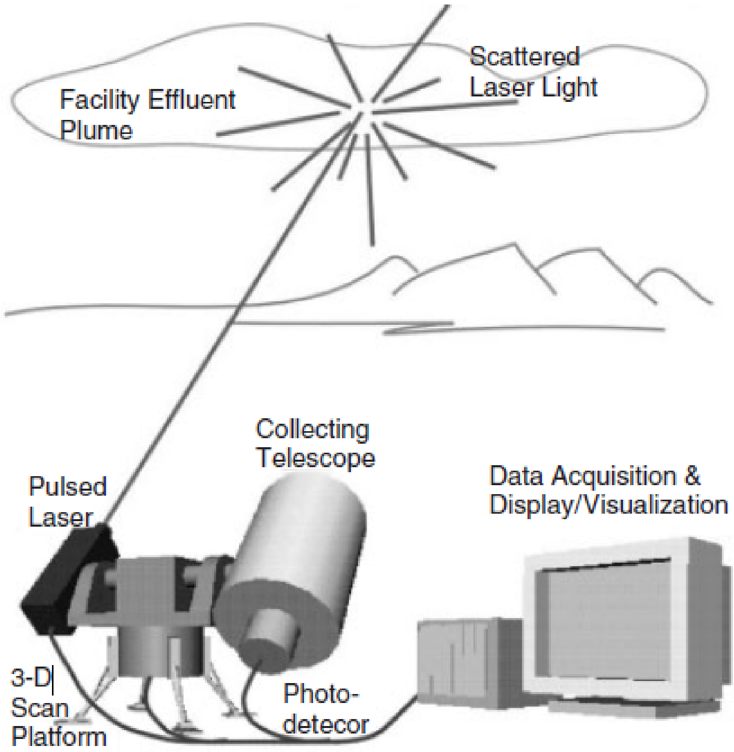

Figure 2.7: A conceptual drawing of the major parts of a lidar system.

2.2.3 Lidar Modeling

In this section we present the lidar coordinate system and the lidar models for idealized point measurements and more realistic volume measurements.

Lidar Coordinate System

The lidar measurements are modeled in the lidar coordinate system, which in this work is denoted by the subscript $\mathcal{L}$. This is necessary, because the lidar system can be installed at different locations other than the origin of the inertial frame or the system can change its position and inclination, for example on the nacelle of an operating wind turbine or on a heavy bouy for offshore applications. All six DOFs are considered as illustrated in the figure below. The position of the lidar system within the inertial coordinate system is defined by $\begin{bmatrix} x_{L,\mathcal{I}} & y_{L,\mathcal{I}} & z_{L,\mathcal{I}} \end{bmatrix}^T$. The rotation follows the convention used in aviation. The translated system is rotated around the z-axis by the yaw angle Ψ_L, around the rotated y-axis by the pitch angle Θ_L, and finally around the rotated x-axis by the roll angle Φ_L.

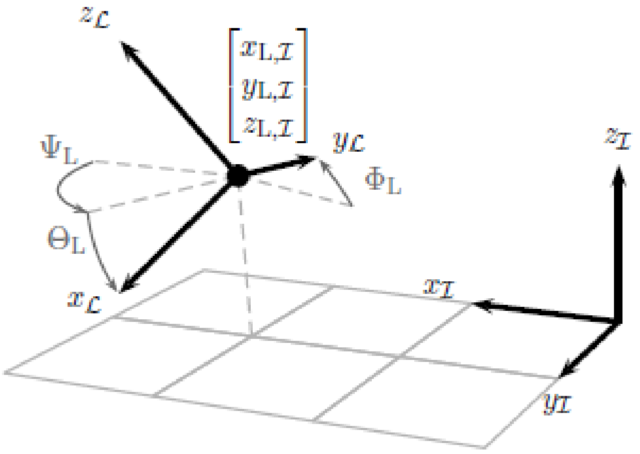

Figure 2.8: Orientation of the lidar coordinate system (subscript $\mathcal{L}$) in the inertial coordinate (subscript $\mathcal{I}$): Origin of the $\mathcal{L}$-system within the $\mathcal{I}$-system is $[u_{L,\mathcal{I}} \quad v_{L,\mathcal{I}} \quad w_{L,\mathcal{I}}]^T$ and the rotation order from $\mathcal{L}$ to $\mathcal{I}$ is defined as yaw → pitch → roll ($\Psi_L \rightarrow \Theta_L \rightarrow \Phi_L$).

The transformation from the lidar to the inertial coordinate system is then calculated with the rotation matrix $\mathbf{T}_{\mathcal{I}\mathcal{L}}$ by

$$\begin{bmatrix} x_{i,\mathcal{I}} \\ y_{i,\mathcal{I}} \\ z_{i,\mathcal{I}} \end{bmatrix} = \mathbf{T}_{\mathcal{I}\mathcal{L}} \begin{bmatrix} x_{i,\mathcal{L}} \\ y_{i,\mathcal{L}} \\ z_{i,\mathcal{L}} \end{bmatrix} + \begin{bmatrix} x_{L,\mathcal{I}} \\ y_{L,\mathcal{I}} \\ z_{L,\mathcal{I}} \end{bmatrix} \tag{2.24}$$

with

$$\mathbf{T}_{\mathcal{I}\mathcal{L}} = \underbrace{\begin{bmatrix} \cos(\Psi_L) & -\sin(\Psi_L) & 0 \\ \sin(\Psi_L) & \cos(\Psi_L) & 0 \\ 0 & 0 & 1 \end{bmatrix}}_{T_{\text{yaw}}} \underbrace{\begin{bmatrix} \cos(\Theta_L) & 0 & \sin(\Theta_L) \\ 0 & 1 & 0 \\ -\sin(\Theta_L) & 0 & \cos(\Theta_L) \end{bmatrix}}_{T_{\text{pitch}}} \underbrace{\begin{bmatrix} 1 & 0 & 0 \\ 0 & \cos(\Phi_L) & -\sin(\Phi_L) \\ 0 & \sin(\Phi_L) & \cos(\Phi_L) \end{bmatrix}}_{T_{\text{roll}}} \tag{2.25}$$

and the transformation back to the lidar coordinate system by

$$\begin{bmatrix} x_{i,\mathcal{L}} \\ y_{i,\mathcal{L}} \\ z_{i,\mathcal{L}} \end{bmatrix} = \mathbf{T}_{\mathcal{L}\mathcal{I}} \begin{bmatrix} x_{i,\mathcal{I}} - x_{L,\mathcal{I}} \\ y_{i,\mathcal{I}} - y_{L,\mathcal{I}} \\ z_{i,\mathcal{I}} - z_{L,\mathcal{I}} \end{bmatrix} \quad \text{with } \mathbf{T}_{\mathcal{L}\mathcal{I}} = \mathbf{T}_{\mathcal{I}\mathcal{L}}^{-1} \tag{2.26}$$

Lidar Model for Point Measurement

A lidar system is only able to measure the component of the wind vector in the laser beam direction. Per convention this value is positive, if the wind is directed towards the laser source. Therefore, the line-of-sight wind speed $V_{\mathrm{los},i}$ measured at point i with coordinates $\begin{bmatrix} x_{i,\mathcal{I}} & y_{i,\mathcal{I}} & z_{i,\mathcal{I}} \end{bmatrix}^T$ can be modeled by a projection of the wind vector $\begin{bmatrix} u_{i,\mathcal{I}} & v_{i,\mathcal{I}} & w_{i,\mathcal{I}} \end{bmatrix}^T$ at point i and the normalized vector of the backscattered laser beam, which mathematically is equivalent to the scalar product of both vectors:

$$V_{\mathrm{los},i} = x_{n,i,\mathcal{I}} u_{i,\mathcal{I}} + y_{n,i,\mathcal{I}} v_{i,\mathcal{I}} + z_{n,i,\mathcal{I}} w_{i,\mathcal{I}} \tag{2.27}$$

where the normalized laser vector measuring at a distance r_{Li} from the lidar system is

$$\begin{bmatrix} x_{n,i,\mathcal{I}} \\ y_{n,i,\mathcal{I}} \\ z_{n,i,\mathcal{I}} \end{bmatrix} = \frac{1}{r_{Li}} \begin{bmatrix} x_{L,\mathcal{I}} - x_{i,\mathcal{I}} \\ y_{L,\mathcal{I}} - y_{i,\mathcal{I}} \\ z_{L,\mathcal{I}} - z_{i,\mathcal{I}} \end{bmatrix} \text{ with } r_{Li} = \sqrt{x_{i,\mathcal{L}}^2 + y_{i,\mathcal{L}}^2 + z_{i,\mathcal{L}}^2} \tag{2.28}$$

This model is independent of the used coordinate system. However, it is more convenient to use the $\mathcal{I}$-system. If the lidar system is not fixed in the inertial frame $\begin{bmatrix} \dot{x}_{L,\mathcal{I}} & \dot{y}_{L,\mathcal{I}} & \dot{z}_{L,\mathcal{I}} \end{bmatrix}^T$, Eq. (2.27) can be adjusted as follows:

$$V_{\mathrm{los},i} = x_{n,i,\mathcal{I}}(u_{i,\mathcal{I}} - \dot{x}_{L,\mathcal{I}}) + y_{n,i,\mathcal{I}}(v_{i,\mathcal{I}} - \dot{y}_{L,\mathcal{I}}) + z_{n,i,\mathcal{I}}(w_{i,\mathcal{I}} - \dot{z}_{L,\mathcal{I}}) \tag{2.29}$$

Lidar Model for Volume Measurement

In the equation for $V_{\mathrm{los},i}$, the measurement is assumed for one single point. However, real lidar systems measure within a probe volume due to the length of the emitted pulse of pulsed lidar systems [22] or due to the focusing of the laser beam of continuous wave lidar systems [23]. Additionally, the FFT involved in the direction of the frequency shift requires a certain fraction of the backscattered signal, contributing to the averaging effect. Thus, lidar measurements are modeled more realistically considering the overall averaging effect by:

$$V_{\mathrm{los},i} = \int_{-\infty}^{\infty} (x_{n,i,\mathcal{I}} u_{a,i,\mathcal{I}} + y_{n,i,\mathcal{I}} v_{a,i,\mathcal{I}} + z_{n,i,\mathcal{I}} w_{a,i,\mathcal{I}}) f_{RW}(a) \mathrm{d}a \tag{2.30}$$

The range weighting function $f_{RW}(a)$ at the distance a to the measurement point depends on the used lidar technology (pulsed or continuous wave). The wind vector $\begin{bmatrix} u_{a,i,\mathcal{I}} & v_{a,i,\mathcal{I}} & w_{a,i,\mathcal{I}} \end{bmatrix}^T$ is an evaluation of the wind field at

$$\begin{bmatrix} x_{a,i,\mathcal{I}} \\ y_{a,i,\mathcal{I}} \\ z_{a,i,\mathcal{I}} \end{bmatrix} = \begin{bmatrix} x_{i,\mathcal{I}} \\ y_{i,\mathcal{I}} \\ z_{i,\mathcal{I}} \end{bmatrix} + a \begin{bmatrix} x_{n,i,\mathcal{I}} \\ y_{n,i,\mathcal{I}} \\ z_{n,i,\mathcal{I}} \end{bmatrix} \tag{2.31}$$

Again, Eq. (2.30) can be adjusted for moving lidar systems similar to Eq. (2.29):

$$V_{\text{los},i} = \int\limits_{-\infty}^{\infty} (x_{n,i,\mathcal{I}}(u_{a,i,\mathcal{I}} - \dot{x}_{L,\mathcal{I}}) + y_{n,i,\mathcal{I}}(v_{a,i,\mathcal{I}} - \dot{y}_{L,\mathcal{I}}) + z_{n,i,\mathcal{I}}(w_{a,i,\mathcal{I}} - \dot{z}_{L,\mathcal{I}}))f_{RW}(a)\text{d}a \tag{2.32}$$

For the pulsed lidar system considered in this research, a normalized Gaussian shape weighting function is used (see figure below) following [22]. The function is parameterized by a standard deviation σ_L depending on the Full Width at Half Maximum (FWHM) of $W_L = 30$m:

$$f_{RW}(a) = \frac{1}{\sigma_L\sqrt{2\pi}} \exp\left(-\frac{a^2}{2\sigma_L^2}\right) \text{ with } \sigma_L = \frac{W_L}{2\sqrt{2\ln 2}} \tag{2.33}$$

Following the considerations of [23], a normalized Lorentzian shape weighting function is used to model the volume measurement of continuous-wave lidar systems. This is given by

$$f_{RW}(a) = \frac{\Gamma_L/\pi}{a^2 + \Gamma_L^2} \text{ with } \Gamma_L = \frac{\lambda_L r_{Li}^2}{\pi A_L^2} \tag{2.34}$$

Here Γ_L is the halfwidth of the weighting function at the -3 dB point depending on the beam radius at the output lens $A_L = 28$mm, the laser wavelength λ_L, and the focus range r_{Li}. Figure shows the function for $r_{Li} = 100$m.

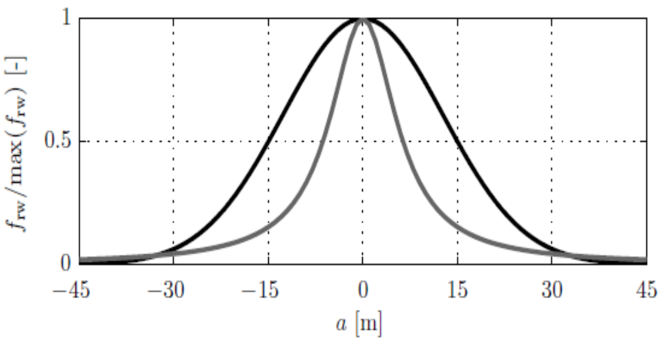

Figure 2.9: Normalized range weighting functions for a pulsed lidar system (black) and a continuous-wave lidar system (gray) at a focus range of 100m.

2.3 Correlation between Wind Systems and LiDAR Systems

The applications of lidar to wind measurement were first explored in the 1980's. This earlier applications consist of lidar systems that were too large, complex and expensive to be widely used. Lidar technology has become more and more popular for site assessment purpose since 2003, coinciding with the development of a new generation of lidar devices based on components that have been originated from the telecommunication industry.

In an attempt to make wind lidars more applicable for mass-production and broad industrial use, collaboration between Windar Photonics A/S and DTU Fotonik in 2008 led to the first demonstration of a low-cost, compact wind lidar based on an all semiconductor laser source [24]. The first successful field deployment of such system was demonstrated by the same group in 2012 [25].

Lidar systems in wind energy applications are mainly used to measure wind speeds. This can be done by simulated lidar measurements in which the lidar system scans the wind field taking into account the movement of the lidar system on the nacelle and the blockage effect of the rotating blades based on the system states of the simulated turbine. The simulator calculates the line-of-sight wind speed and a signal quality flag similar to a real lidar system. The lidar simulator then transfers the raw lidar data to the lidar-assisted controller, where the data is finally processed together with the wind turbine outputs to control the wind turbine.

Therefore, for lidar assisted control, it is crucial to know the correlation between the wind speed preview provided by a nacelle- or spinner-based lidar system and the wind speed affecting the turbine. If on the one side the assumed correlation is overestimated, the uncorrelated frequencies of the preview will cause unnecessary control action, inducing undesired loads. On the other side the benefits of the lidar-assisted controller will not be fully exhausted, if correlated frequencies are filtered out.

However, there are several interacting effects which determine how well the wind speed is predicted. One of these is the Kaimal wind spectra [50] used to model the correlation between lidar systems and wind turbines. The correlation is expressed by the magnitude squared coherence γ^2_{RL} between the rotor effective wind speed measured by the lidar and that sensed by the turbine's rotor, defined as

$$\gamma^2_{RL} = \frac{|S_{RL}|^2}{S_{RR}S_{LL}} \tag{2.35}$$

where S_{RL}, S_{RR}, and S_{LL} are the cross-spectrum between both signals and the auto-spectrum of the signal from the turbine and the lidar, respectively.

CHAPTER 3

MODELS AND METHODOLOGY

3.1 Classical Model

3.1.1 Structural Mechanics

The main purpose of a structural model of a wind turbine is to be able to determine the temporal variation of the material loads in the various components in order to estimate the fatigue damage. Further, a dynamic system is used when analyzing the stability of the wind turbine design, including perhaps the control system. To calculate the deflections and velocities of the various components in the wind turbine in the time domain, a structural model including the inertia terms is needed. Then the dynamic structural response of the entire construction can be calculated subject to the time dependent load found using an aerodynamic model. For offshore wind turbines, wave loads and perhaps ice loads on the bottom of the tower must also be estimated [26]. We proceed by presenting a detail approach of setting up the structural model based on the principle of virtual work. The velocity of the vibrating wind turbine construction must be subtracted when calculating the relative velocity seen locally by the blade. The loads therefore depend on the deflections and velocities of the structure, which again depend on the loads. The structural and aerodynamic models are therefore highly coupled and must be solved together in what is known as aeroelastic problem.

3.1.2 Modal shape functions and Principle of Virtual Work

The principle of virtual work is a method to set up the correct mass matrix, **M**, stiffness matrix **K**, and damping matrix **C**, for a discretized mechanical system as:

$$\mathbf{M}\ddot{\mathbf{x}} + \mathbf{C}\dot{\mathbf{x}} + \mathbf{K}\mathbf{x} = \mathbf{F_g} \tag{3.1}$$

where $\mathbf{F_g}$ denotes the generalized force vector associated with the external loads, $\mathbf{p}$. Eq. (3.1) is of course nothing but Newton's second law, assuming linear stiffness and damping, and the method of virtual work is nothing but a method that helps in setting up the correct mass, stiffness and damping matrices for a multi-body system, which is especially well suited for a chain system. Knowing the loads and appropriate conditions for the velocities and the deformations, Eq. (3.1) can be solved for the accelerations, from which the velocities and deformations can be estimated for the next time step. The number of elements in $\mathbf{x}$ is called the number of degrees of freedom, DOF, and the higher this number the more computational time is needed in each time step to solve the matrix system. Use of modal shape functions is a tool to reduce the number of degrees of freedom and thus reduce the size of the matrices to make computations faster per time step. A deflection shape in this method is described as a linear combination of a few but physically realistic basis functions, which are often the deflection shapes corresponding to the eigenmodes with the lowest eigenfrequencies. For a wind turbine such an approach is suited to describe the deflection of the rotor blades and the assumption is that the combination of the power spectral density of the loads and the damping of the system do not excite eigenmodes associated with higher frequencies.

The values in the vector $\mathbf{x}$ describing the deformation of the construction, x_i, are known as the general coordinates. To each generalized coordinate is associated a deflection shape, $\mathbf{u}_{\boldsymbol{i}}$, that describes the deformation of the construction when only x_i is different from zero and typically has a unit value. The element i in the generalized force corresponding to a small displacement in DOF number i, $\mathrm{d}x_i$, is calculated such that the work done by the generalized force equals the work done on the construction by the distributed external loads on the associated deflection shape:

$$F_{g,i}\,\mathrm{d}x_i = \int \mathbf{p} \cdot \mathbf{u}_{\boldsymbol{i}}\,\mathrm{d}S \tag{3.2}$$

where S denotes the entire system. The generalized force can be a moment and the displacement can be angular. All loads must be included, in other words also gravity and inertial loads such as Coriolis, centrifugal and gyroscopic loads. The non-linear centrifugal stiffening can be modelled as equivalent loads calculated from the local centrifugal force and the actual deflection shape. The elements in the mass matrix, $m_{i,j}$, can be evaluated as the generalized force from the inertia loads from a unit acceleration of DOF j for a unit displacement of DOF i. The elements in the stiffness matrix, $k_{i,j}$, correspond to the generalized force from an external force field which keeps the system in equilibrium for a unit displacement in DOF j and which then is displaced $x_i = 1$. The elements in the damping matrix can be found similarly. For a chain system the method of virtual work as described here normally gives a full mass matrix and diagonal matrices for the stiffness and damping.

If the structural system comprises a system of continuous mass distributions, such as a system of beams, Eq. (3.1) is the result of discretizing the system, since in reality such a system has an infinite number of DOFs. The elements in the mass, stiffness and damping matrices depend on the system and, in the case of a continuous system, also of the discretization. If the right hand side of Eq. (3.1) is zero the system is said to perform its natural motion.

Provided that the deflections, $\mathbf{x}$, and velocities $\dot{\mathbf{x}}$, are known, Eq. (3.1) can be alternatively written as:

$$\mathbf{M}\ddot{\mathbf{x}} = \mathbf{F_g} - \mathbf{C}\dot{\mathbf{x}} - \mathbf{K}\mathbf{x} = \mathbf{f}(\dot{\mathbf{x}}, \mathbf{x}, t) \tag{3.3}$$

where the function $\mathbf{f}$ in general is non-linear. Non-linearity can come, for example, from non-linear loads $\mathbf{p}$ or from aerodynamic damping. A non-linear system can be treated as a linearized eigenvalue approach or as a full non-linear time domain approach.

Knowing the right hand side of Eq. (3.3) at time $t^n = n\Delta t$, the acceleration at time t^n is found solving the linear system of equations:

$$\ddot{\mathbf{x}} = \mathbf{M}^{-1}\mathbf{f}(\dot{\mathbf{x}}^n, \mathbf{x}^n, t^n) \tag{3.4}$$

Knowing the accelerations, $\ddot{\mathbf{x}}^n$, the velocities, $\dot{\mathbf{x}}^n$, and positions, $\mathbf{x}^n$, at time t^n, an iterative scheme can be used to estimate the velocities, $\dot{\mathbf{x}}^{n+1}$, and positions, $\mathbf{x}^{n+1}$, at t^{n+1}. New loads, $\mathbf{p}^{n+1}(\dot{\mathbf{x}}^{n+1}, \mathbf{x}^{n+1}, t^{n+1})$, can be calculated using, for example, an unsteady BEM method and thus Eq. (3.4) can be updated and a new time step can be performed. This can be continued until a sufficient time period has been simulated.

3.1.3 Cyclic Loading

The three most important source of the loading of a wind turbine are [26]:

- Gravitational loading;
- Inertial loading; and
- Aerodynamic loading

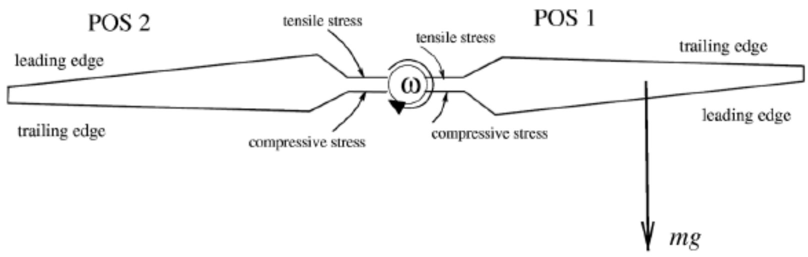

Figure 3.1: The loading caused by the Earth's gravitational field

Gravitational Loading:

The Earth's gravitational field causes a sinusoidal gravitational loading on each blade, as indicated in figure 3.1

When the blade is in position 1 (down-rotating) the blade root at the trailing edge side is exposed to tensile stress and the leading edge side of the blade root is exposed to compressive stress. In position 2 (up-rotating) the trailing edge side of the blade root is exposed to compressive stress and the leading edge side of the blade root is exposed to tensile stress. Thus gravity is responsible for a sinusoidal loading of the blades with a frequency corresponding to the rotation of the rotor often denoted by 1P[1]. This loading is easily recognized in the time series of the edgewise bending moment. Note that a wind turbine is designed to operate for 20 years, which means that a machine operating at 25 rpm will be exposed to $20 \times 365 \times 24 \times 60 \times 25 = 2.6 \times 10^8$ stress cycles from gravity. Since a wind turbine blade might weigh several tons and be more than 30 m long, the stresses from the gravity loading are very important in the fatigue analysis.

Inertial Loading

Inertial loading occurs when, for example, the turbine is accelerated or decelerated. An example is the braking of the rotor, where a braking torque T is applied at the rotor shaft. A small section of the blade will feel a force $\mathrm{d}F$ in the direction of the rotation as indicated in figure 3.2a.

The size of dF is found from:

$$\mathrm{d}F = \dot{\omega} r m \mathrm{d}r \tag{3.5}$$

[1] A frequency of 1P (one-per-revolution) is equivalent to 0.202Hz

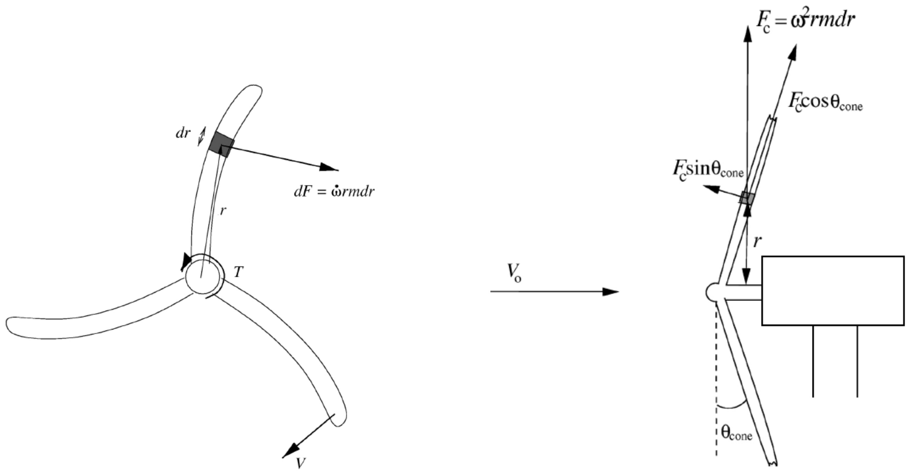

(a) Loading caused by rotor braking **(b)** Effect of coning the rotor

Figure 3.2: Inertial loading

where m is the mass per length of the blade, r the blade radius from the rotational axis to the section and $\mathrm{d}r$ the size of the small section; $\dot{\omega} = \mathrm{d}\omega/\mathrm{d}t$ can be found from:

$$I\frac{\mathrm{d}\omega}{\mathrm{d}t} = T \tag{3.6}$$

where I is the moment of inertia of the rotor.

Another inertial loading stems from the centrifugal force on the blades. In order to reduce the flapwise bending moment, the rotor can be coned backwards with a cone angle of θ_{cone} as shown in figure 3.2b.

The centrifugal force acting on the incremental part of the blade at a radius r from the rotational axis as shown above is $F_c = \omega^2 rm\mathrm{d}r$, where M is the mass of the incremental part and ω the angular velocity of the rotor. Due to the coning the centrifugal force has a component in the spanwise direction of the blade, $F_c \cos\theta_{\text{cone}}$, and a component normal to the blade, $F_c \sin\theta_{\text{cone}}$, as shown in the figure. The normal component gives a flapwise bending moment in the opposite direction to the bending moment caused by the thrust and thus reduces the total flapwise bending moment.

Aerodynamic Loading

The aerodynamic loading is caused by the flow past the structure, in other words the blade and the tower. The wind field seen by the rotor varies in space and time due to atmospheric turbulence as sketched in figure 3.3.

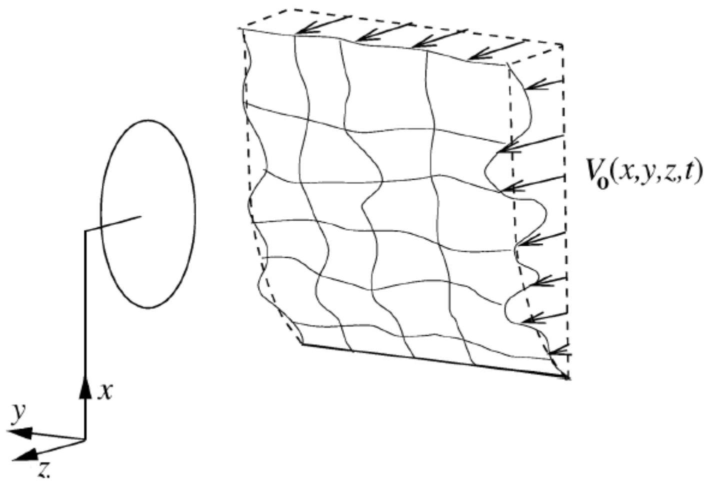

Figure 3.3: Sketch of turbulent inflow seen by wind turbine rotor

Mean wind speed is also a function of height. The ground, even in the absence of obstacles, produces friction forces that delay the winds in the lower layers. This phenomenon, called wind shear, is more appreciable as height decreases and has important effects on wind turbine operation. Different mathematical models have been proposed to describe wind shear. One of them is the Prandtl logarithmic law [27].

$$\frac{V_m(z)}{V_m(z_{\mathrm{ref}})} = \frac{\ln(z/z_0)}{\ln(z_{\mathrm{ref}}/z_0)} \tag{3.7}$$

where z is the height above the ground level, z_{ref} is the reference height (usually 10m) and z_0 is the roughness length. Typical values of this parameter for different types of terrain are listed in the table 3.1. Another empirical formula often used to describe the effect of the terrain on the wind speed gradient is the following exponential law [28]:

$$V_m(z) = V_m(z_{\mathrm{ref}}) \left(\frac{z}{z_{\mathrm{ref}}}\right)^{\alpha} \tag{3.8}$$

Where the surface roughness exponent α is also a terrain-dependent parameter. Values of α for different types of surface are presented in the last column of the table 3.1.

Type of surface	z_0(mm)	α
sand	0.2 to 0.3	0.10
mown grass	1 to 10	0.13
high grass	40 to 100	0.19
suburb	1000 to 2000	0.32

Table 3.1: Typical values of roughness length z_0 and roughness exponent α for different types of surface [28, 29].

3.2 Fluid Mechanical Models

In a fluid with no individual solid particles it is common to consider a fixed volume in space, denoted as a control volume (CV). Newton's second law is:

$$\boldsymbol{F} = \frac{\mathrm{d}\boldsymbol{P}}{dt} \tag{3.9}$$

where $\boldsymbol{F} = (F_x, F_y, F_z)$ is the total force, $\boldsymbol{P}$ is the momentum and t is the time. The time derivative of the momentum is found from integrating over the control volume as:

$$\frac{\mathrm{d}\boldsymbol{P}}{dt} = \frac{\partial}{\partial t}\iiint\limits_{\mathrm{CV}} \rho\boldsymbol{q}\,\mathrm{d}V + \iint\limits_{\mathrm{CS}} \boldsymbol{q}\rho\boldsymbol{q}\cdot\mathrm{d}\mathbf{A} \tag{3.10}$$

where ρ is the density, $\boldsymbol{q}$ is the velocity, $\mathrm{d}V$ is an infinitesimal part of the total control volume, CS denotes the surface of the control volume and $\mathrm{d}\mathbf{A}$ is a normal vector to an infinitesimal part of the control surface. The length of $\mathrm{d}\mathbf{A}$ is the area of this infinitesimal part. Newton's second law for the control volume then becomes:

$$\boldsymbol{F} = \frac{\partial}{\partial t}\iiint\limits_{\mathrm{CV}} \rho\boldsymbol{q}\,\mathrm{d}V + \iint\limits_{\mathrm{CS}} \boldsymbol{q}\rho\boldsymbol{q}\cdot\mathrm{d}\mathbf{A} \tag{3.11}$$

where $\boldsymbol{F}$ is the total external force including the pressure and viscous forces acting on the control surfaces. Further, body forces, for example gravity, and forces from the flow past an object inside the control volume contribute to the total force. Eq. 3.11 is normally used to determine an unknown force, provided that the velocity is known at the control surfaces. When Stoke's hypothesis for an incompressible fluid, Eqs. (3.12) – (3.17), is used for the stresses on an infinitesimal control volume with side lengths $(\mathrm{d}x, \mathrm{d}y, \mathrm{d}z)$, the three partial differential momentum Eqs. (3.19) – (3.21) are derived. The first subscript on τ indicates the face where the stress is located; the second subscript is the direction of the stress:

$$\tau_{xx} = -p + 2\mu\frac{\partial u}{\partial x} \tag{3.12}$$

$$\tau_{xy} = \tau_{yx} = \mu \left(\frac{\partial u}{\partial y} + \frac{\partial v}{\partial x} \right) \tag{3.13}$$

$$\tau_{xz} = \tau_{zx} = \mu \left(\frac{\partial u}{\partial z} + \frac{\partial w}{\partial x} \right) \tag{3.14}$$

$$\tau_{yy} = -p + 2\mu \frac{\partial v}{\partial y} \tag{3.15}$$

$$\tau_{yz} = \tau_{zy} = \mu \left(\frac{\partial v}{\partial z} + \frac{\partial w}{\partial y} \right) \tag{3.16}$$

$$\tau_{zz} = -p + 2\mu \frac{\partial w}{\partial z} \tag{3.17}$$

$p(x, y, z, t)$ denotes the pressure, $\boldsymbol{q}(x, y, z, t) = (u, v, w)$ are the velocity components $\mathbf{x} = (x, y, z)$ are the coordinates in a Cartesian frame of reference and μ is the viscosity.

The three momentum Eqs. (3.19) – (3.21) plus the continuity equation Eq. (3.18) comprise the Navier-Stokes equations for an incompressible fluid with constant viscosity μ:

$$\frac{\partial u}{\partial x} + \frac{\partial v}{\partial y} + \frac{\partial w}{\partial z} = 0 \tag{3.18}$$

$$\rho \left(\frac{\partial u}{\partial t} + u\frac{\partial u}{\partial x} + v\frac{\partial u}{\partial y} + w\frac{\partial u}{\partial z} \right) = -\frac{\partial p}{\partial x} + \mu \left(\frac{\partial^2 u}{\partial x^2} + \frac{\partial^2 u}{\partial y^2} + \frac{\partial^2 u}{\partial z^2} \right) + f_x \tag{3.19}$$

$$\rho \left(\frac{\partial v}{\partial t} + u\frac{\partial v}{\partial x} + v\frac{\partial v}{\partial y} + w\frac{\partial v}{\partial z} \right) = -\frac{\partial p}{\partial y} + \mu \left(\frac{\partial^2 v}{\partial x^2} + \frac{\partial^2 v}{\partial y^2} + \frac{\partial^2 v}{\partial z^2} \right) + f_y \tag{3.20}$$

$$\rho \left(\frac{\partial w}{\partial t} + u\frac{\partial w}{\partial x} + v\frac{\partial w}{\partial y} + w\frac{\partial w}{\partial z} \right) = -\frac{\partial p}{\partial z} + \mu \left(\frac{\partial^2 w}{\partial x^2} + \frac{\partial^2 w}{\partial y^2} + \frac{\partial^2 w}{\partial z^2} \right) + f_z \tag{3.21}$$

Eq. (3.18) ensures that the net mass flow is zero in and out of an infinitesimal box with side lengths dx, dy, dz. Eqs. (3.19) – (3.21) are Newton's second law, in the x, y and z direction respectively, for an infinitesimal box in the fluid, which is fixed in space. The left hand side terms are the inertial forces and the right hand side terms are the pressure forces, the viscous forces and the external body forces $\mathbf{f}(x, y, z, t) = (f_x, f_y, f_z)$ acting on the box respectively. Eq. (3.18) and Eqs. (3.19) – (3.21) can also be written in vector notation as:

$$\nabla \cdot \boldsymbol{q} = 0 \tag{3.22}$$

$$\rho\left(\frac{\partial \boldsymbol{q}}{\partial t}+(\boldsymbol{q}\cdot\nabla)\boldsymbol{q}\right)=-\nabla p+\mu\nabla^2\boldsymbol{q}+\mathbf{f} \tag{3.23}$$

If no external forces are present and if the flow is stationary and the viscous forces are zero, Eq. (3.23) reduces to:

$$-\frac{\nabla p}{\rho}=(\boldsymbol{q}\cdot\nabla)\,\boldsymbol{q}=\frac{1}{2}\nabla\,(\boldsymbol{q}\cdot\boldsymbol{q})-\boldsymbol{q}\times(\nabla\times\boldsymbol{q}) \tag{3.24}$$

The last equality in Eq. (3.24) above comes from a vector identity. If the flow is irrotational, i.e. $\nabla\times\boldsymbol{q}=0$, the Bernoulli equation (3.25) follows directly from Eq. (3.24) and is valid between any two points in the flow domain:

$$p+\frac{1}{2}\rho\left(u^2+v^2+w^2\right)=\text{constant} \tag{3.25}$$

If the flow is not irrotational, it can be shown from Eq. (3.24) that the Bernoulli Eq. (3.25) is still valid, but only along a streamline. To use the Bernoulli equation it is necessary that the flow is stationary, that no external forces are present and that the flow is incompressible and frictionless. The Bernoulli equation is generally valid along a streamline, but if the flow is irrotational, the equation is valid between any two points.

The Navier-Stokes equations are difficult to solve and often the integral formulation Eq. (3.11) is used in engineering problems. If the flow is stationary and the torque on the sides of an annular control volume is zero, the integral moment of momentum becomes:

$$\mathbf{M}=\iint \boldsymbol{r}\times\boldsymbol{q}\rho\boldsymbol{q}\cdot\mathrm{d}\mathbf{A} \tag{3.26}$$

where $\mathbf{M}$ is an unknown torque acting on the fluid in the control volume and r is the radius from the cylindrical axis. If the flow is uniform at the inlet and exit of the control volume and the only non-zero component of $\mathbf{M}$ is in the flow direction z, Euler's turbine equation Eq. (3.27) can be derived from Eq. (3.26) [30]:

$$P=M_z\omega=\omega\dot{m}\left(r_1V_{0,1}-r_2V_{0,2}\right) \tag{3.27}$$

P is the power removed from the flow on a mechanical shaft, ω is the rotational speed of the shaft, V_0 is the tangential velocity component, $\dot{m}$ is the mass flow through the control volume, and subscripts 1 and 2 denote the inlet and exit of the control volume respectively.

Another important equation is the integral conservation of energy or the first law of thermodynamics for a control volume, which for steady flow is:

$$P+Q=\iint\left(u_i+\frac{p}{\rho}+\frac{1}{2}(u^2+v^2+w^2)\right)\rho\boldsymbol{q}\cdot\mathrm{d}\mathbf{A} \tag{3.28}$$

where P and Q are the mechanical power and the rate of heat transfer added to the control volume and u_i is the internal energy.

3.2.1 Rotational Effects

This sections deals with the effects of blade rotation on the aerodynamics.

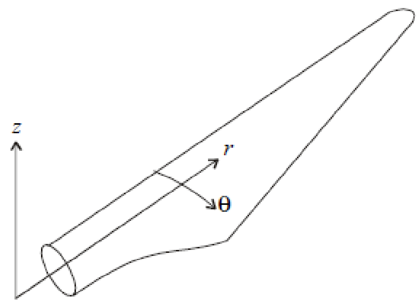

Figure 3.4: The blade in the rotating frame of reference.

When it is assumed that the flow about a wind turbine blades is incompressible and that the viscous stress is linearly proportional to the velocity gradients, which are both generally accepted assumptions, the fundamental continuity equation and the Navier-Stokes equation for the velocity $\boldsymbol{q}$ are already given above. To apply these equations to the situation of a rotating wind turbine blade and owing to the geometry of the lidar beams, we choose to work in cylindrical polar coordinates defined by radial r, azimuthal θ and vertical z-directions. For the continuity equation this yields:

$$\frac{\partial q_r}{\partial r} + \frac{q_r}{r} + \frac{1}{r}\frac{\partial q_\theta}{\partial \theta} + \frac{\partial q_z}{\partial z} = 0 \tag{3.29}$$

and the atmospheric boundary-layer flow is governed by the incompressible Navier-Stokes equations [31], given by (Figure 3.4):

$$\frac{\partial q_r}{\partial t} + q_r\frac{\partial q_r}{\partial r} + \frac{q_\theta}{r}\frac{\partial q_r}{\partial \theta} - \frac{q_\theta^2}{r} + q_z\frac{\partial q_r}{\partial z} = f_r - \frac{1}{\rho}\frac{\partial p}{\partial r} + \frac{\mu}{\rho}\left(\frac{\partial^2 q_r}{\partial r^2} + \frac{1}{r}\frac{\partial q_r}{\partial r} + \frac{1}{r^2}\frac{\partial^2 q_r}{\partial \theta^2} + \frac{\partial^2 q_r}{\partial z^2}\right) \tag{3.30}$$

$$\frac{\partial q_\theta}{\partial t} + q_r\frac{\partial q_\theta}{\partial r} + \frac{q_\theta}{r}\frac{\partial q_\theta}{\partial \theta} - \frac{q_r q_\theta}{r} + q_z\frac{\partial q_\theta}{\partial z} = f_\theta - \frac{1}{\rho r}\frac{\partial p}{\partial \theta} + \frac{\mu}{\rho}\left(\frac{\partial^2 q_\theta}{\partial r^2} + \frac{1}{r}\frac{\partial q_\theta}{\partial r} + \frac{1}{r^2}\frac{\partial^2 q_\theta}{\partial \theta^2} + \frac{\partial^2 q_\theta}{\partial z^2}\right) \tag{3.31}$$

$$\frac{\partial q_z}{\partial t} + q_r \frac{\partial q_z}{\partial r} + \frac{q_\theta}{r} \frac{\partial q_z}{\partial \theta} + q_z \frac{\partial q_z}{\partial z} = f_z - \frac{1}{\rho} \frac{\partial p}{\partial z} + \frac{\mu}{\rho} \left(\frac{\partial^2 q_z}{\partial r^2} + \frac{1}{r} \frac{\partial q_z}{\partial r} + \frac{1}{r^2} \frac{\partial^2 q_z}{\partial \theta^2} + \frac{\partial^2 q_z}{\partial z^2} \right) \tag{3.32}$$

3.2.2 Forces in the Rotating Frame of Reference

For an incompressible fluid with only one phase, the external forces in the inertial (non-rotating) reference system are usually zero. In practice the only external force is gravitational, but that force is balanced by the hydrostatic pressure gradient, so that both are left out of the equations. In a rotating frame the centrifugal and Coriolis forces appear. An observer on the blade notices radial and azimuthal accelerations on passing air elements $\mathrm{d}\lambda$. Therefore the centrifugal and Coriolis forces are real forces in the rotating frame of reference. If the angular velocity of the frame of reference is Ω then the centrifugal force equals $\rho \mathrm{d}\lambda \Omega^2 r$. When the particle is moving in the rotating system with velocity vector $\mathbf{v}$, then the Coriolis force equals $2\rho \mathrm{d}\lambda \mathbf{\Omega} \times v$. The vector $\mathbf{\Omega}$ only has a z-component, and thus the Coriolis accelerations are: $2v_r\Omega\hat{\theta} - 2v_\theta\Omega\hat{r}$, in which $\hat{\theta}$ and $\hat{r}$ are the unit vectors in the θ and r-direction respectively. They act on the mass element in addition to other inertial forces, which, however can be left out, as explained above. So, the Coriolis force acts in the θ-direction and r-direction, and thus the first term on the right hand side of the azimuth equation of motion above can be replaced by $2v_r\Omega$. As the centrifugal force works in the r-direction, the first term on the right hand side of the radial equation of motion can be replaced by a centrifugal contribution $r\Omega^2$ and a Coriolis contribution $-2v_\theta\Omega$. In the above it is assumed that the wing rotates in the r, θ-plane given by $z = 0$. But in practice the rotor blades have a small cone angle and therefore the tip rotates at a slightly negative value of z. The centrifugal and Coriolis force are thus assumed to work in the plane of the boundary layer. In short, the relevant external force per unit of mass are:

$$F_\theta = 2v_r\Omega, \quad F_r = r\Omega^2 - 2v_\theta\Omega, \quad F_z = 0 \tag{3.33}$$

3.2.3 Boundary Layer Assumptions

In the flow about rotating wind turbine blades the rate of downstream convection (in the θ-direction) is much larger than the rate of transverse viscous diffusion, which means that viscosity only plays a significant role in a thin so-called boundary layer around the object. This insight will be used to estimate the order of magnitude of terms in the continuity equation and the equations of motion. Terms of small order will then be neglected.

The thickness of the boundary layer can be estimated as follows. At the wall the velocity is 0 and at a certain distance, say δ, perpendicular to the wall the flow velocity will be v_θ. The velocity gradient perpendicular to the wall is therefore approximately v_θ/δ and the shear stress $\tau = -\mu v_\theta/\delta$. The derivative of this stress $\partial\tau/\partial y$ equals the convective deceleration of the flow $\rho v_\theta/r(\partial v_\theta/\partial\theta)$, where $\partial v_\theta/\partial\theta = v_\theta/(c/r)$ and c is the chord of the airfoil. Thus $\partial\tau/\partial y = -\mu v_\theta/\delta^2 = \rho v_\theta^2/c$, or $\delta = \sqrt{\mu c/\rho v_\theta}$, which is very small since $\mu_{\text{air}} = 17.1 \times 10^{-6}$ Pas. It follows that the shear layer of thickness δ is small compared to the chord $c = r\theta$. The z-direction is perpendicular to the boundary layer where most velocity changes take place. The velocity derivatives in the z-direction are therefore relatively large: $\partial v_\theta/\partial z$ is of order v_θ/δ. Outside the boundary layer the second derivative of v_θ in the z-direction is zero. Thus inside the boundary layer the second derivative equals the change of the first derivative, which was of the order v_θ/δ. Therefore the second derivative $\partial^2 v_\theta/\partial z^2$ is of order v_θ/δ^2. These results will be used to find the significant terms which yield the boundary layer equations.

3.2.4 Attached Flow on a Rotating Blade

For a wind turbine blade with attached flow, a typical value for the ratio of the tip speed ΩR and the axial wind speed V, $\lambda = \Omega R/V$, is approximately 7. That means that the inflow speed is close to the speed of the blade element itself being given by radial position times the angular speed. This is true for radial positions of approximately $0.3R$ and larger. In this range the pressure distribution on the blade is roughly proportional to $\rho v_\theta^2/2$, which is approximately $\rho\Omega^2 r^2/2$. The radial pressure gradient will therefore be approximately $\rho\Omega^2 r$ and due to this pressure gradient an element of air in the boundary will be accelerated in the radial direction with an acceleration of approximately $\Omega^2 r$. The given element will remain approximately $c/v_\theta = c/(\Omega r)$ in the boundary layer and thus will develop a radial speed v_r of approximately $\Omega^2 rc/(\Omega r) = \Omega c$. Thus the order of magnitude of v_r is Ωc and, in a similar way, $\partial v_r/\partial z$ and $\partial^2 v_r/\partial z^2$ are found to be of the order $\Omega c/\delta$ and $\Omega c/\delta^2$ respectively.

By substitution of v_θ and v_r in the continuity equation and assuming $r \gg c$ it follows that v_z is approximately $\Omega r\delta/c$, because it should balance the largest term which is $\partial v_\theta/(r\partial\theta)$. Table 3.2 list all estimates.

Parameter	Estimate	Parameter	Estimate	Parameter	Estimate
δ	$\sqrt{\mu c/\rho v_\theta}$	p	$\rho\Omega^2 r^2/2$	$\partial p/\partial r$	$\rho\Omega^2 r$
v_θ	Ωr	$\partial v_\theta/\partial z$	$\Omega r/\delta$	$\partial^2 v_\theta/\partial z^2$	$\Omega r/\delta^2$
v_r	Ωc	$\partial v_r/\partial z$	$\Omega c/\delta$	$\partial^2 v_r/\partial z^2$	$\Omega c/\delta^2$
v_z	$\Omega r\delta/c$	$\partial v_z/\partial z$	$\Omega r/c$	$\Delta\theta$	c/r

Table 3.2: Parameters and order of magnitude

Now the Navier-Stokes equations can be written in terms of estimates instead of derivatives and unspecified forces. We will do so by giving the order of magnitude under each term. The order of magnitude of the pressure terms follows from the equations and is therefore set by the other terms. For the equation of continuity and those of θ, r and z-motion respectively, it follows that:

3.3 Quantum Mechanical Model

The non-relativistic time-dependent Schrödinger equation of an N-electron atom (ion) in the Schrödinger picture and in the position representation reads:

$$i\hbar\frac{\partial}{\partial t}\Psi(\mathbf{x}_i,t) = H(t)\Psi(\mathbf{x}_i,t) \tag{3.34}$$

where $\Psi(\mathbf{x}_i,t)$ is the wavefunction written with space-spin coordinates ($\{\mathbf{x}_i\} = \{\boldsymbol{r}_i,\sigma_i\}$, $i = 1,\ldots,N$) (with $\boldsymbol{r}_i \in \mathbb{R}^3$ and $\sigma_i = \uparrow$ or $\downarrow$) and time t. $H(t)$ is the semi-classical Hamiltonian describing the atomic system in the presence of the radiation field, which in the Coulomb gauge is given by:

$$H(t) = H_0 + H_{\text{int}}(t) \tag{3.35}$$

where the time-independent Hamiltonian H_0 for a real material consisting of N electrons and M nuclei in the absence of electromagnetic field is given by

$$\begin{aligned} H_0 = &\sum_{\alpha=1}^{M}\frac{\hbar^2}{2M_\alpha}\nabla_\alpha^2 - \sum_{i=1}^{N}\frac{\hbar^2}{2m_e}\nabla_i^2 + \sum_{i<j}\frac{e^2}{4\pi\epsilon_0|\boldsymbol{r}_i-\boldsymbol{r}_j|} - \sum_{i,\alpha}\frac{Z_\alpha e^2}{4\pi\epsilon_0|\boldsymbol{r}_i-\mathbf{R}_\alpha|} \\ &+ \sum_{\alpha<\beta}\frac{Z_\alpha Z_\beta e^2}{4\pi\epsilon_0|\mathbf{R}_\alpha-\mathbf{R}_\beta|} \end{aligned} \tag{3.36}$$

Here $\mathbf{R}_\alpha$, Z_α, and M_α are the position, charge and mass of the α–th nucleus respectively and $\boldsymbol{r}_i$ is the position of the ith electron, with mass m and charge (magnitude)

e. If we invoke the Born-Oppenheimer approximation [32], which is valid when electrons reach equilibrium on a time scale that is short compared to the time scale on which the nuclei move, we arrive at

$$\begin{aligned} H_0 &= -\sum_{i=1}^{N} \frac{\hbar^2}{2m_e}\nabla_i^2 + \frac{1}{2}\sum_{i,j}\frac{e^2}{4\pi\epsilon_0|\boldsymbol{r}_i - \boldsymbol{r}_j|} - \sum_{i,\alpha}\frac{Z_\alpha e^2}{4\pi\epsilon_0|\boldsymbol{r}_i - \mathbf{R}_\alpha|} \\ &= \frac{1}{2m_e}\sum_{i=1}^{N}\boldsymbol{p}_i^2 + V \end{aligned} \tag{3.37}$$

$\boldsymbol{p}_i = i\hbar\nabla_i$ is the momentum operator in the position representation of the ith electron and V denotes the Coulomb interactions within the atomic system in the absence of the radiation field.

The interaction Hamiltonian $H_{\text{int}}(t)$ is given by

$$H_{\text{int}}(t) = \frac{e}{m_e}\sum_{i=1}^{N}\boldsymbol{A}(\boldsymbol{r}_i, t)\cdot\boldsymbol{p}_i + \frac{e^2}{2m_e}\sum_{i=1}^{N}\boldsymbol{A}^2(\boldsymbol{r}_i, t) \tag{3.38}$$

3.3.1 Quantum Scattering

To gain information about the nature of the approaching wind, it is important to study the scattering of the incident lidar by the wind particles.

Suppose the lidar is incident within an infinitesimal patch of cross-sectional area $\mathrm{d}\sigma$ and scatters into a corresponding infinitesimal solid angle $\mathrm{d}\Omega$, then $\mathrm{d}\sigma$ is proportional to $\mathrm{d}\Omega$ and the proportionality factor $\mathrm{d}\sigma/\mathrm{d}\Omega$ is called the differential (scattering) cross-section. The differential cross-section gives the number of particles scattered into the element of solid angle $\mathrm{d}\Omega$ around Ω, divided by $\mathrm{d}\Omega$ and by the number of incident particles per unit area

$$\frac{\mathrm{d}\sigma}{\mathrm{d}\Omega} = \frac{1}{N_{\text{in}}}\frac{\mathrm{d}N(\Omega)}{\mathrm{d}\Omega} \tag{3.39}$$

Here, N_{in} signifies the number of incident particles and $\mathrm{d}N(\Omega)$ the number of particles scattered into the element of solid angle $\mathrm{d}\Omega$.

In the quantum theory of scattering[2], the particle incident on a target that is producing an outgoing spherical wave is usually represented by plane wave $\psi(z) = Ae^{ikz}$, travelling in the z direction. So that the solution to the Schrödinger equation are generally of the form

$$\psi(r,\theta,\phi) = A\left\{e^{ikz} + f(\theta,\phi)\frac{e^{ikr}}{r}\right\} \quad \text{for large } r \tag{3.40}$$

[2]See, for example, Griffiths Introduction to Quantum Mechanics

where the wave number k is related to the energy of incident particles in the usual way:

$$k = \frac{\sqrt{2mE}}{\hbar} \tag{3.41}$$

and $f(\theta, \phi)$ is the scattering amplitude.

The whole problem is to determine the scattering amplitude $f(\theta, \phi)$; which tells us the probability of scattering in a given direction, and hence is related to the differential cross-section. Indeed, the probability that the incident particle, traveling at speed v, passes through the infinitesimal area $\mathrm{d}\sigma$, in time $\mathrm{d}t$, is

$$\mathrm{d}P = |\psi_{\text{in}}|^2 \mathrm{d}V = |A|^2 (v\mathrm{d}t)\mathrm{d}\sigma \tag{3.42}$$

But this is equal to the probability that the particle scatters into the corresponding solid angle $\mathrm{d}\Omega$:

$$\mathrm{d}P = |\psi_{\text{sca}}|^2 \mathrm{d}V = \frac{|A|^2|f|^2}{r^2}(v\mathrm{d}t)r^2\mathrm{d}\Omega \tag{3.43}$$

From which it follows that $\mathrm{d}\sigma = |f|^2\mathrm{d}\Omega$ and hence

$$\frac{\mathrm{d}\sigma}{\mathrm{d}\Omega} = |f(\theta, \phi)|^2 \tag{3.44}$$

Evidently, the differential cross-section (which is the quantity of interest) is equal to the absolute square of the scattering amplitude. The total scattering cross section σ is given by the integral of the last equation above over all angles:

$$\sigma = \int \mathrm{d}\Omega |f(\theta, \phi)|^2 \tag{3.45}$$

3.3.2 Lidar Equation

In the simplest form, the detected lidar signal can be written as [15]

$$P(r) = KG(r)\beta(r)T(r) \tag{3.46}$$

where P is the power received from a distance r, K summarizes the performance of the lidar system and is called the lidar system constant, $G(r)$ describes the range-dependent measurement geometry. The term $\beta(r)$ is the backscatter coefficient at distance r. It stands for the ability of the atmosphere to scatter light back into the direction from which it comes. $T(r)$ is the transmission term and describes how much light gets lost on the way from the lidar to distance r and back. In more details, we can write the system constant as

$$K = P_0 \frac{c\tau}{2} A\eta \tag{3.47}$$

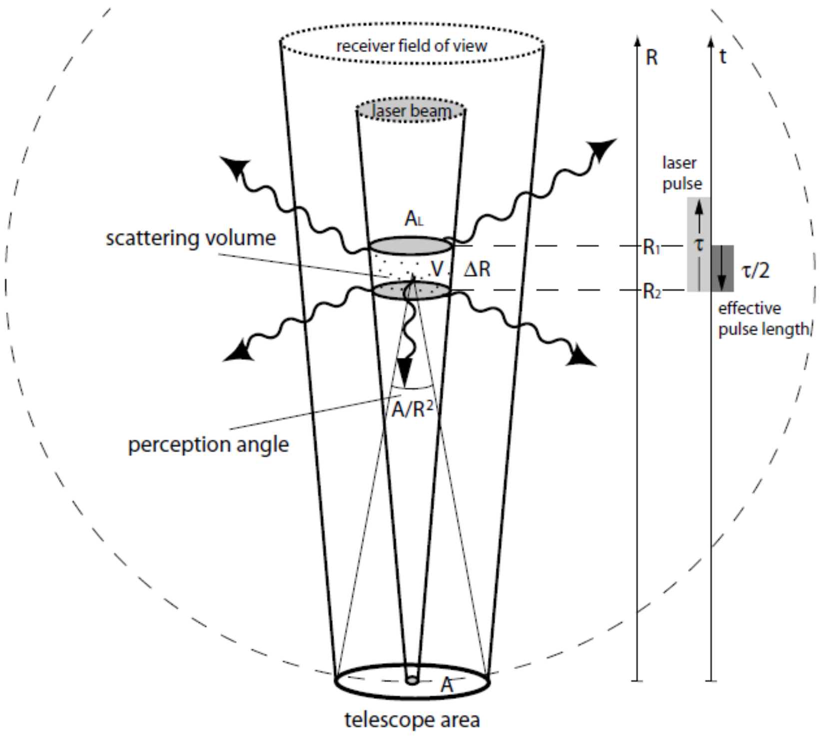

Figure 3.5: Illustration of the lidar geometry [15].

where P_0 and τ are the average power and the temporal pulse length of a single laser pulse respectively. Hence $E_0 = P_0\tau$ is the pulse energy, and $c\tau$ is the length of the volume illuminated by the laser pulse at a fixed time. The factor $1/2$ appears due to an apparent "folding" of the laser pulse through the backscatter process as illustrated in the diagram. When the lidar signal is detected at an instant of time t after the leading edge of the pulse comes from the distance $r_1 = ct/2$. At the same time, light produced by the trailing edge arrives from the distance $r_2 = c(t-\tau)/2$. Thus $\Delta r = r_1 - r_2 = c\tau/2$ is the length of the volume from which backscattered light is received at an instant time and is called the "effective (spatial) pulse length." A is the area of the primary receiver optics responsible for the collection of backscattered light, and η is the overall system efficiency. It includes the optical frequency of all elements the transmitted and received light has to pass and the detection efficiency. The telescope area A and the laser energy E_0, or, rather, the average laser power $\bar{P} = E_0 f_{\text{rep}}$, with the pulse repetition frequency f_{rep}, are primary design parameters of a lidar system.

The geometric factor

$$G(r) = \frac{\mathcal{O}(r)}{r^2} \tag{3.48}$$

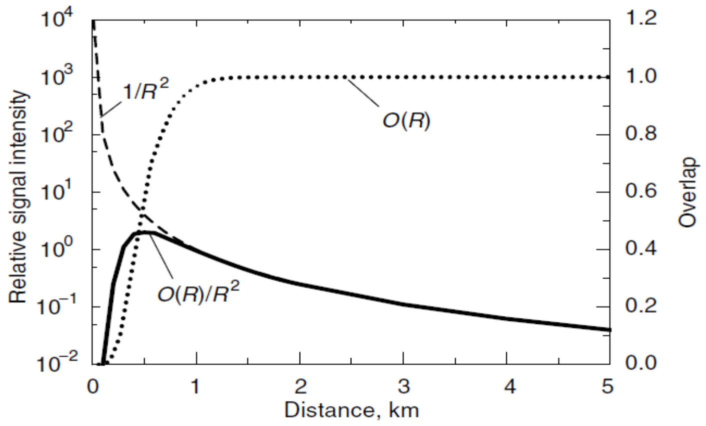

Figure 3.6: Influence of the overlap function on the signal dynamics.

includes the laser-beam receiver-field-of-view overlap function $\mathcal{O}(r)$ described before and the term r^{-2}. The inverse square relationship of the signal intensity with distance is due to the fact that the receiver telescope area makes up part of a sphere's surface with radius r that encloses the scattering volume (see figure 3.5). If we imagine an isotropic scatterer at distance r, the telescope area A will collect the fraction

$$\frac{I_c}{I_s} = \frac{A}{4\pi r^2} \tag{3.49}$$

of the overall intensity I_s scattered into the solid angle 4π. In other words, the solid angle A/r^2 is the perception angle of the lidar for light scattered at distance r. It is primarily the r^{-2} dependence that is responsible for the large dynamic range of the lidar signal. If we start detecting a signal with $\mathcal{O}(r) = 1$ at a distance of 10m, the signal will be of 6 orders of magnitude lower at 10km distance just because of the geometry effect. To what extent lidar is a *range-resolving and remote* measurement technique depends on our ability to compensate for this effect. Geometrical signal compression at short distances is one possibility as can be seen from the figure below in which an arbitrary, but realistic overlap function is shown, multiplied with the function r^{-2}. The strong signal in the near field is suppressed by several orders of magnitude. On a few occasions the atmosphere will help in compressing the signal by an increase of the backscattering at larger distances. In most cases, however, the atmosphere causes an additional decrease of the signal with range.

The backscatter coefficient $\beta(r, \lambda)$ is the primary atmospheric parameter that determines the strength of the lidar signal. It describes how much light is scattered into the backward direction, i.e., towards the lidar receiver. The backscatter coefficient is the specific value of the scattering coefficient for the scattering angle $\theta = 180°$. Let N_j be the concentration of scattering particles of kind j in the volume illuminated by the laser pulse, and $\mathrm{d}\sigma_{j,\mathrm{sca}}(\pi, \lambda)/\mathrm{d}\Omega$ the particles' differential scattering cross section for the backward direction at wavelength λ. The backscatter coefficient can then be written as

$$\beta(r, \lambda) = \sum_j N_j(r) \frac{\mathrm{d}\sigma_{j,\mathrm{sca}}}{\mathrm{d}\Omega}(\pi, \lambda) \tag{3.50}$$

with summing over all kinds of scatterers. Since the number concentration is given in units of m^{-3} and the differential scattering cross section in $\mathrm{m}^2\ \mathrm{sr}^{-1}$, the backscatter coefficient has the unit $\mathrm{m}^{-1}\ \mathrm{sr}^{-1}$.

In a simplified version of isotropic scattering we assume that there is only one type of particle in the scattering volume, the relation between the backscatter coefficient and the isotropic scattering cross section σ_{sca} is $4\pi\beta = N\sigma_{\mathrm{sca}}$. For a laser-beam cross section A_L, the intensity of the scattered light from the illuminated volume $V = A_L \Delta r = A_L c\tau/2$ is proportional to the area $A_s = N\sigma_{\mathrm{sca}} V$, i.e., the scattering cross section of all particles in the volume V. Thus, the relative intensity of the scattered light is

$$\frac{I_s}{I_0} = \frac{A_s}{A_L} = \frac{N\sigma_{\mathrm{sca}} c\tau}{2} = \frac{4\pi\beta c\tau}{2} \tag{3.51}$$

with Eq. (3.49), we obtain the ratio of the collected to the emitted light intensity

$$\frac{I_c}{I_0} = \frac{A\beta c\tau}{2r^2} \tag{3.52}$$

The right side of this equation describes that part of the lidar equation that directly refers to the scattering geometry, i.e., it contains the size and the backscatter properties of the scattering volume and the perception angle of the lidar.

In the atmosphere, the laser light is scattered by air molecules and particulate matter, i.e., $\beta(r, \lambda)$ can be written as

$$\beta(r, \lambda) = \beta_{\mathrm{mol}}(r, \lambda) + \beta_{\mathrm{aer}}(r, \lambda) \tag{3.53}$$

Molecular scattering (index mol), mainly occurring from nitrogen and oxygen molecules, primarily depends on air density and thus decreases with height. Particulate scattering (index aer for aerosol particles) is highly variable in the atmosphere on all spatial and temporal scales.

As the final part of the lidar equation, we have to consider the fraction of light that gets lost on the way from the lidar to the scattering volume and back. The transmission term $T(r)$ can take values between 0 and 1 and is given by:

$$T(r,\lambda) = \exp\left[-2\int_0^r \alpha(r',\lambda)\mathrm{d}r'\right] \tag{3.54}$$

This term results from the specific form of the Lambert-Beer-Bouguer law for lidar [33, 34]. The integral considers the path from the lidar to distance r. The factor 2 stands for the two-way transmission path. The sum of all transmission losses is called light extinction, and $\alpha(r,\lambda)$ is the extinction coefficient. It is defined in a similar way as the backscatter coefficient as the product of number concentration and extinction cross section $\sigma_{j,\mathrm{ext}}$ for each type of scatterer j,

$$\alpha(r,\lambda) = \sum_j N_j(r)\sigma_{j,\mathrm{ext}}(\lambda) \tag{3.55}$$

Extinction can occur because of scattering and absorption of light by molecules and particles. The extinction coefficient therefore can be written as the sum of four components,

$$\alpha(r,\lambda) = \alpha_{\mathrm{mol,sca}}(r,\lambda) + \alpha_{\mathrm{mol,abs}}(r,\lambda) + \alpha_{\mathrm{aer,sca}}(r,\lambda) + \alpha_{\mathrm{aer,abs}}(r,\lambda) \tag{3.56}$$

where the indices sca and abs stand for scattering and absorption respectively. Because scattering into all directions contributes to light extinction, the (integral) scattering cross section σ_{sca}, together with the absorption cross section σ_{abs}, both in m^2, make up the extinction cross section,

$$\sigma_{\mathrm{ext}}(\lambda) = \sigma_{\mathrm{sca}}(\lambda) + \sigma_{\mathrm{abs}}(\lambda) \tag{3.57}$$

Consequently, the extinction coefficient has the unit m^{-1}.

As indicated in the equations above, both β and α depend on the wavelength of the laser light. This wavelength dependence is determined by the size, the refractive index, and the shape of the scattering particles. Summarizing the discussion of the individual terms, we can now write the lidar equation in a more common form as

$$P(r,\lambda) = P_0\frac{c\tau}{2}A\eta\frac{\mathcal{O}(r)}{r^2}\beta(r,\lambda)\exp\left[-2\int_0^r \alpha(r',\lambda)\mathrm{d}r'\right] \tag{3.58}$$

A common and a simplified method of solution to the lidar equation above called the slope method is based on the assumption that the atmosphere is homogeneous. In many cases, the atmospheric horizontal homogeneity is a reasonable assumption. A simple mathematical solution for Eq. (3.58) is achievable for the unknown extinction coefficient α if the examined atmosphere is considered to be homogeneous. For a valid homogeneous atmosphere solution, the following two conditions must be met:

$$\alpha(r) = \text{constant} \tag{3.59}$$

and

$$\beta(r) = \text{constant} \tag{3.60}$$

So the lidar equation for homogeneous atmosphere then reduces to

$$P(r) = \frac{K\beta}{r^2} e^{-2\alpha r} \tag{3.61}$$

The term $1/r^2$ in the lidar equation causes the measured signal $P(r)$ to diminish sharply with range because of the decreasing solid angle subtended by the receiving telescope with range. To compensate for this effect, the lidar signal $P(r)$ is commonly transformed into a range-corrected signal before lidar signal inversion is begun. This is accomplished by multiplying the original signal $P(r)$ by the square of the range, r^2 and denoting it by $S(r)$. So,

$$S(r) = r^2 P(r) = K\beta e^{-2\alpha r} \tag{3.62}$$

Taking the logarithm of the transformed signal and denoting it as $\Phi(r)$, we have

$$\Phi(r) = \ln\left(r^2 P(r)\right) = \ln(K) + \ln(\beta(r)) - 2\alpha(r)r \tag{3.63}$$

The linear dependence of $\Phi(r)$ on range r is a key factor when seeking the simplest solution to the lidar equation [35]. On differentiating Eq. (3.63) with respect to r we obtain the nonlinear differential equation

$$\frac{\mathrm{d}\Phi(r)}{\mathrm{d}r} = \frac{1}{\beta(r)} \frac{\mathrm{d}\beta(r)}{\mathrm{d}r} - 2\alpha(r) \tag{3.64}$$

which for homogeneous media reduces to

$$\alpha = -\frac{1}{2} \frac{\mathrm{d}\Phi(r)}{\mathrm{d}r} \tag{3.65}$$

A linear fit where $\Phi(r)$ is a straight line allows the determination of the attenuation coefficient α in a least square sense.

For inhomogeneous media, it is customary to assume a relation of between extinction and the backscatter term of the form [36]

$$\beta(r) = C\alpha^u(r) \tag{3.66}$$

where both C and u are constants. Using Eq. (3.66) in Eq. (3.64), we have

$$\frac{u}{\alpha(r)}\frac{\mathrm{d}\alpha(r)}{\mathrm{d}r} - 2\alpha(r) = \frac{1}{S(r)}\frac{\mathrm{d}S(r)}{\mathrm{d}r} \tag{3.67}$$

which is a nonlinear ODE of elementary structure known as the homogeneous Riccati equation. The solution is

$$\alpha(r) = \frac{S(r)^{1/u}}{S(r_f)^{1/u}/\alpha(r_f) + \dfrac{2}{u}\displaystyle\int_r^{r_f} S(r')^{1/u}\mathrm{d}r'} \tag{3.68}$$

where r_f is the range at which the boundary value $\alpha(r_f)$ is specified. The integral term in the denominator of Eq. (3.68) is positive if $r_f > r$ but negative if $r_f < r$. Also the solution is independent of K if K is independent of r. The major problem with this solution is that it is unstable in media of moderate to high density unless the boundary value is given at the far end of the measurable lidar return [37] where, however, it is less likely to be known. In addition, the solution (3.68) rests on the validity of Eq. (3.66) which means that the size distribution and composition of the scattering particles must change in a prescribed manner within the medium–the inhomogeneities being solely caused by fluctuations in number density.

3.3.3 Elastic-Backscattered Lidar

In its simplest form, the lidar equation for return signals due to elastical backscatter by air molecules and aerosol particles, can be written as [38]:

$$P(r) = \frac{E_0\eta_L}{r^2}\mathcal{O}(r)\beta(r)\exp\left[-2\int_0^r \alpha(r')\mathrm{d}r'\right] \tag{3.69}$$

$P(r)$ is the signal owing to Rayleigh and particle scattering received from distance r, E_0 is the transmitted laser pulse energy, η_L contains lidar parameters describing the efficiencies of the optical and detection units, $\mathcal{O}(r)$ describes the overlap between the outgoing laser beam and the receiver field of view. Backscattering $\beta(r)$ (in $\mathrm{km}^{-1}\mathrm{sr}^{-1}$) and extinction $\alpha(r)$ (in km^{-1}) are both caused by particles and molecules with molecular absorption effects ignored:

$$\beta(r) = \beta_{\mathrm{mol}}(r) + \beta_{\mathrm{aer}}(r) \tag{3.70}$$

$$\alpha(r) = \alpha_{\mathrm{mol}}(r) + \alpha_{\mathrm{aer}}(r) \tag{3.71}$$

The above equations can be summarized to

$$S(r) = E_0\eta_L\left[\beta_{\mathrm{mol}}(r) + \beta_{\mathrm{aer}}(r)\right]\exp\left[-2\int_0^r \left[\alpha_{\mathrm{mol}}(r') + \alpha_{\mathrm{aer}}(r')\right]\mathrm{d}r'\right] \tag{3.72}$$

with the range-corrected lidar signal $S(r) = r^2 P(r)$. The overlap is assumed to be complete $[\mathcal{O}(r) \equiv 1]$, i.e., the minimum distance r_{min} at which measurements can be made may be defined by $\mathcal{O}(r) \leq 1$ for $r \leq r_{\mathrm{min}}$. The molecular scattering properties, $\beta_{\mathrm{mol}}(r)$ and $\alpha_{\mathrm{mol}}(r)$, can be determined from the best available meteorological data of temperature and pressure or approximated from appropriate standard atmospheres so that only the aerosol scattering and absorption properties $\beta_{\mathrm{aer}}(r)$ and $\alpha_{\mathrm{aer}}(r)$, remain to be determined.

Next we introduce the particle extinction-to-backscatter ratio (lidar ratio)

$$L_{\mathrm{aer}}(r) = \frac{\alpha_{\mathrm{aer}}(r)}{\beta_{\mathrm{aer}}(r)} \tag{3.73}$$

in analogy to the molecular lidar ratio

$$L_{\mathrm{mol}}(r) = \frac{\alpha_{\mathrm{mol}}(r)}{\beta_{\mathrm{mol}}(r)} = \frac{8\pi}{3}\,\mathrm{sr} \tag{3.74}$$

In contrast to the molecular lidar ratio, the particle lidar ratio is range-dependent because it depends on the size distribution, shape, and chemical composition of the particles.

The primary information contained in the measured elastic lidar returns is the backscatter coefficient under typical tropospheric conditions with particle vertical optical depth of ≤ 0.3 in the visible spectrum around 550 nm. Under these conditions only the backscatter coefficient can be derived with good accuracy from the elastic backscatter signal. So we introduce the term [39]

$$Y(r) = L_{\mathrm{aer}}(r)[\beta_{\mathrm{mol}}(r) + \beta_{\mathrm{aer}}(r)] \tag{3.75}$$

After substituting $\alpha_{\mathrm{aer}}(r)$ and $\alpha_{\mathrm{mol}}(r)$ in Eq. (3.72) with the expressions (3.73) and (3.74) and inserting $Y(r)$ from Eq. (3.75), the resulting equation can be written as

$$\begin{aligned} S(r)L_{\mathrm{aer}}(r)\exp\left\{-2\int_0^r [L_{\mathrm{aer}}(r') - L_{\mathrm{mol}}(r')]\beta_{\mathrm{mol}}(r')\mathrm{d}r'\right\} \\ = E_0\eta_L Y(r)\exp\left[-2\int_0^r Y(r')\mathrm{d}r'\right] \end{aligned} \tag{3.76}$$

Taking the logarithms of both sides of Eq. (3.76) and differentiating them with respect to r gives

$$\begin{aligned} \frac{\mathrm{d}}{\mathrm{d}r}\ln\left(S(r)L_{\mathrm{aer}}(r)\exp\left\{-2\int_0^r [L_{\mathrm{aer}}(r') - L_{\mathrm{mol}}(r')]\beta_{\mathrm{mol}}(r')\mathrm{d}r'\right\}\right) \\ = \frac{1}{Y(r)}\frac{\mathrm{d}Y(r)}{\mathrm{d}r} - 2Y(r) \end{aligned} \tag{3.77}$$

Eq. (3.77) known as the Bernoulli equation is usually solved for the boundary condition

$$Y(r_0) = L_{\text{aer}}(r_0)[\beta_{\text{aer}}(r_0) + \beta_{\text{mol}}(r_0)] \tag{3.78}$$

to obtain [38]:

$$\beta_{\text{aer}}(r) + \beta_{\text{mol}}(r) = \frac{S(r)L_{\text{aer}}(r)\exp\left\{-2\int_{r_0}^{r}[L_{\text{aer}}(r') - L_{\text{mol}}(r')]\beta_{\text{mol}}(r')\mathrm{d}r'\right\}}{\dfrac{S(r_0)}{\beta_{\text{aer}}(r_0) + \beta_{\text{mol}}(r_0)} - 2\displaystyle\int_{r_0}^{r} L_{\text{aer}}(r')S(r')T(r', r_0)\mathrm{d}r'} \tag{3.79}$$

where

$$T(r, r_0) = \exp\left\{-2\int_{r_0}^{r}[L_{\text{aer}}(r') - L_{\text{mol}}(r')]\beta_{\text{mol}}(r')\mathrm{d}r'\right\} \tag{3.80}$$

The profile of the particle extinction coefficient can be estimated from the solution $\beta_{\text{aer}}(r)$ by

$$\alpha_{\text{aer}}(r) = L_{\text{aer}}(r)\beta_{\text{aer}}(r) \tag{3.81}$$

Eq. (3.79) can, in principle, be integrated by starting from the reference range r_0, which may be either the near end ($r > r_0$, forward integration) or the remote end ($r < r_0$, backward integration) of the measuring range. Numerical stability, which is not to be mistaken for accuracy, is, however, given only in the backward integration case [37].

3.4 Correlation models and algorithm for field reconstruction

Pulsed lidars provide radial wind components on different lines of sight at different altitudes. In an ideal case, and to mimic local sensors such as cup or sonic anemometers, beams intersect at the point of interest within a small volume. In an operational situation, only one lidar is available. To reconstruct the 3D components of the wind field, we make the following assumptions [40, 41]:

- Horizontal homogeneity: the three components of the wind are the same for the different points of the disc at a given altitude. The numerous measurement campaigns have proven that this assumption is valid on flat terrains and offshore, but not perfect on complex terrains (hills, mountains, forest boarders)

- Temporal variations are slower than the inter-beam distance divided by the horizontal wind speed. This time increases with altitude and matches the conical geometry.

The Doppler beam swinging (DBS) technique is used for the scanning configuration. DBS is used in pulsed lidars to average more information on the LOS. It is used in commercial, ground based lidar systems to retrieve wind speed and wind direction out of the line-of-sight measurement for site assessment. The orthogonal frame of the Windcube [60] is described in figure 3.7.

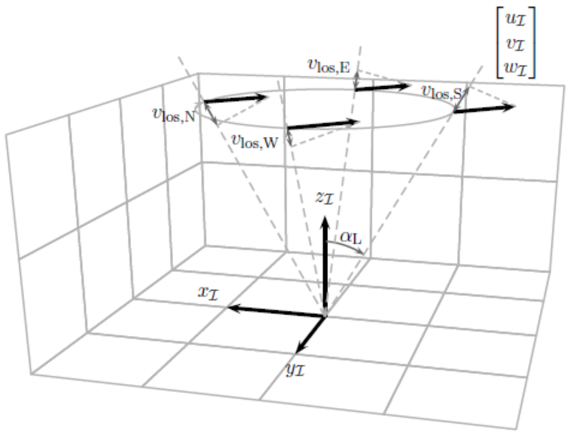

Figure 3.7: Sketch of the DBS scan

Suppose the lidar probes the atmosphere in the four geographic directions with a half opening angle (the so-called cone-angle) of α_L and assuming point measurement (Eq. (2.27)), then the four line-of-sight wind speeds are:

$$V_{\text{los,N}} = u_{\text{N},\mathcal{I}} \sin\alpha_L + w_{\text{N},\mathcal{I}} \cos\alpha_L \tag{3.82a}$$

$$V_{\text{los,W}} = v_{\text{W},\mathcal{I}} \sin\alpha_L + w_{\text{W},\mathcal{I}} \cos\alpha_L \tag{3.82b}$$

$$V_{\text{los,S}} = -u_{\text{S},\mathcal{I}} \sin\alpha_L + w_{\text{S},\mathcal{I}} \cos\alpha_L \tag{3.82c}$$

$$V_{\text{los,E}} = -v_{\text{E},\mathcal{I}} \sin\alpha_L + w_{\text{E},\mathcal{I}} \cos\alpha_L \tag{3.82d}$$

where $u_{\text{N},\mathcal{I}}$ is the longitudinal wind component in the north (N) direction aligned with the $\mathcal{I}$-Coordinate System and accordingly for the other three directions west (W), south (S), and east (E). This system of 4 equations has 8 unknowns and thus it is under-determined and no unique solution exists.

The DBS technique uses the homogeneous flow model, i.e., the wind vector $[u_\mathcal{I}\ v_\mathcal{I}\ w_\mathcal{I}]^T$ in the inertial $\mathcal{I}$-coordinate system is the same for each measurement point i. With this wind model, Eq. (3.82) is simplified to

$$V_{\text{los,N}} = u_{\mathcal{I}} \sin\alpha_L + w_{\mathcal{I}} \cos\alpha_L \tag{3.83a}$$

$$V_{\text{los,W}} = v_{\mathcal{I}} \sin\alpha_L + w_{\mathcal{I}} \cos\alpha_L \tag{3.83b}$$

$$V_{\text{los,S}} = -u_{\mathcal{I}} \sin\alpha_L + w_{\mathcal{I}} \cos\alpha_L \tag{3.83c}$$

$$V_{\text{los,E}} = -v_{\mathcal{I}} \sin\alpha_L + w_{\mathcal{I}} \cos\alpha_L \tag{3.83d}$$

Now, Eq. (3.83) consists of 4 equations for 3 unknowns and in general no solution exists. However, in [60] the following approximation is proposed:

$$u_{\text{DBS},\mathcal{I}} = \frac{V_{\text{los,N}} - V_{\text{los,S}}}{2\sin\alpha_L} \tag{3.84a}$$

$$v_{\text{DBS},\mathcal{I}} = \frac{V_{\text{los,W}} - V_{\text{los,E}}}{2\sin\alpha_L} \tag{3.84b}$$

$$w_{\text{DBS},\mathcal{I}} = \frac{V_{\text{los,N}} + V_{\text{los,W}} + V_{\text{los,S}} + V_{\text{los,E}}}{4\cos\alpha_L} \tag{3.84c}$$

The approximation Eq. (3.84) minimizes the sum of the squares of the errors made in every equation. This can be proven re-writing Eq. (3.83) in the following form:

$$\underbrace{\begin{bmatrix} V_{\text{los,N}} \\ V_{\text{los,W}} \\ V_{\text{los,S}} \\ V_{\text{los,E}} \end{bmatrix}}_{\boldsymbol{m}} = \underbrace{\begin{bmatrix} \sin\alpha_L & 0 & \cos\alpha_L \\ 0 & \sin\alpha_L & \cos\alpha_L \\ -\sin\alpha_L & 0 & \cos\alpha_L \\ 0 & -\sin\alpha_L & \cos\alpha_L \end{bmatrix}}_{\boldsymbol{A}} \underbrace{\begin{bmatrix} u_{\mathcal{I}} \\ v_{\mathcal{I}} \\ w_{\mathcal{I}} \end{bmatrix}}_{\boldsymbol{s}} \tag{3.85}$$

The Moore-Penrose pseudoinverse $\boldsymbol{A}^+$ of matrix $\boldsymbol{A}$ is

$$\boldsymbol{A}^+ = \begin{bmatrix} \frac{1}{2\sin\alpha_L} & 0 & \frac{-1}{2\sin\alpha_L} & 0 \\ 0 & \frac{1}{2\sin\alpha_L} & 0 & \frac{-1}{2\sin\alpha_L} \\ \frac{1}{4\cos\alpha_L} & \frac{1}{4\cos\alpha_L} & \frac{1}{4\cos\alpha_L} & \frac{1}{4\cos\alpha_L} \end{bmatrix} \tag{3.86}$$

Cone-angle α_L is a trade-off between lidar velocity resolution and atmospheric homogeneity. The smaller the cone-angle, the better the wind homogeneity but the wind vector projection on every beam is worse. Best values of α_L are demonstrated to be between 15°and 30°. Even in complex terrains, in general wind non homogeneity condition, no better estimation is obtained when reducing the cone-angle [42, 43]

3.5 Wind Fields and Wind Evolution Models

Analyses of lidar system measurement coherence are performed for two types of wind fields. A wind field characteristics of the U.S Great plains region generated by

TurbSim is used to demonstrate the addition of wind evolution to a frozen wind field. A simple exponential form of longitudinal coherence is used to create wind evolution in this wind field. By adjusting a decay parameter, the intensity of wind evolution can be varied. The second wind field analyzed is a large eddy simulation (LES) of a stable boundary layer. All statistics used to calculate measurement coherence for this wind field are based on measurements from the LES wind field.

3.5.1 The Great Plains-Low Level Jet Wind Field

Wind conditions generated by TurbSim using the Great Plains-Low Level Jet (GP_LLJ) spectral model [44] were used in previous studies [45, 46, 47] to evaluate lidar measurements and controller performance. The wind fields are designed to be used with the National Renewable Energy Laboratory's (NREL's) 5-megawatt (MW) turbine model with a hub height of 90m and a rotor radius of 63m. One of these conditions was chosen as a wind field to which wind evolution can be introduced. One of these conditions was chosen as a wind fields to which wind evolution can be introduced. Table 1 summarizes this unstable wind condition at three different heights, including hub height and 50m below and above hub height.

Height (m)	U (m/s)	$u*$ (m/s)	TI_U (%)	TI_V (%)	TI_W (%)
40	12.25	0.598	9.2	9.4	7.2
90	13	0.530	6.6	7.1	5.7
140	13.44	0.425	4.6	5.3	4.4

Table 3.3: A summary of the Unstable Great Plains-Low Level Jet Wind Field Used for Wind Speed Measurement Analysis with the 5-Megawatt (MW) Wind Turbine Model

The spectra of the u, v, and w components of wind speed are shown in figure 3.8 for the heights summarized in Table 3.3. The spectra are included to illustrate some of the trends that can be seen in the measurement coherence results.

For TurbSim's Great Plains-Low Level Jet spectral model, the transverse coherence at a frequency f between points i and j in the yz plane is defined as:

$$\gamma_{i,j}^2(f,l) = \exp\left(-2a_l\sqrt{\left(\frac{fr_{i,j}}{\bar{u}_{i,j}}\right)^2 + (b_l r_{i,j})^2}\right) \tag{3.87}$$

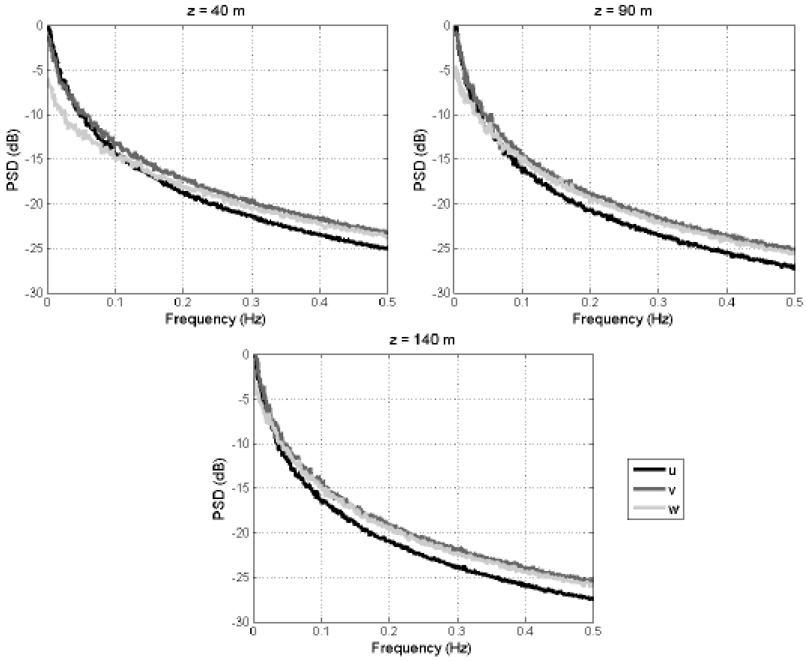

Figure 3.8: Power spectral densities of wind speed components at heights of 40m, 90m, and 140m for the Great Plains-Low Level Jet wind condition (described in Table 3.3).

where

$$r_{i,j} = \text{the distance between the points}$$
$$\bar{u}_{i,j} = \text{the average of the wind speeds at the two points}$$

a_l and b_l are coherence parameters defined for the u, v, and w wind components ($l \in \{u, v, w\}$) [44]

The coherence parameters a_l and b_l are based on field measurements and are $a_u = 9.513$, $a_v = 6.291$, and $a_w = 4.535$ and $b_u = 0.384 \times 10^{-3}$, $b_v = 0.108 \times 10^{-2}$, and $b_w = 0.209 \times 10^{-2}$. The u component of the transverse coherence given by Eq. (3.87) is shown in figure 3.9a for transverse separations in the y direction of 2, 4, 8, 16, and 32m at hub height (z = 90m). This range of distances is indicative of the transverse separations used in calculations of measurement coherence and is described in the next section.

Although the v and w components are correlated as well, the lidar measurement scenarios that are investigated in this report include either u and v components or u and w components, but not both simultaneously. Therefore, the vw correlations are not used in any calculations. Figure 3.9b contains the uw coherence curves for three heights, corresponding to the bottom of the rotor, hub height, and the top of the rotor, as well as the uv coherence function at hub height.

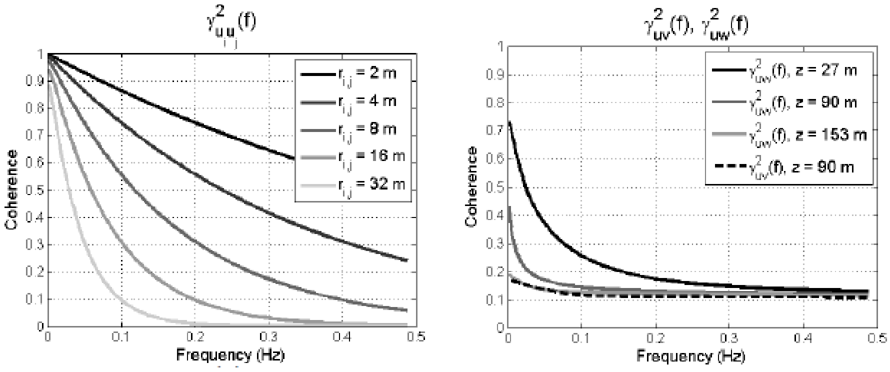

(a) **(b)**

Figure 3.9: Coherence summary for the Great Plains-Low Level Jet wind condition. (a) Transverse coherence functions for the u component at a height of $z = 90$m for transverse separations of 2, 4, 8, 16, and 32m. (b) Coherence between the u and w components of wind at $z = 27$m, 90m, and 153m, which correspond to the bottom of the rotor, the hub height, and the top of the rotor, and coherence between the u and v components at $z = 90$m.

3.5.2 Exponential Wind Evolution Model

A model of wind evolution can be formed using a simple exponential model of coherence that is a function of the non-dimensional product between the eddy wavenumber and longitudinal separation, as suggested in Pielke and Panofsky [48]. This model is given by:

$$\gamma^2(kD) = e^{-akD} \tag{3.88}$$

where

k = the eddy wavenumber ($k = f/U$)

D = the longitudinal separation between points in the wind field

a = a dimensionless decay parameter.

This simple exponential model allows for an easy method of varying the amount of wind evolution by adjusting the decay parameter. Increasing a exaggerates the effects of wind evolution by causing the coherence curve to decay faster with frequency. In section, lidar measurement coherence is calculated for the Great Plains-Low Level Jet wind field using this exponential longitudinal coherence function to describe the evolution of the u, v, and w components for a range of decay parameters between 0.3 and 0.6 in this unstable flow seem to produce roughly the same measurement coherence as the weakly stable LES wind field.

3.5.3 LES Stable Boundary Layer Wind Field

A large eddy simulation of a stable boundary layer [49], provided by the National Center for Atmospheric Research (NCAR), is used to calculate longitudinal coherence curves to model wind evolution. The data is sampled at a rate or roughly 1 hertz (Hz), so the bandwidth used for all the spectral results in this report is approximately 0.5 Hz. The 13-minute LES wind field spans 1000m in the x and y directions, with data existing for heights between 50 and 150m. The spatial resolution is 2m in the x and y directions and 1m in the z direction. A summary of the wind field at heights of 50m, 100m and 150m is provided in Table 3.4. The spectra of the u, v, and w components of wind speed are shown in figure 3.10 for the heights summarized in Table 3.4.

Height (m)	U (m/s)	TI_U (%)	TI_V (%)	TI_W (%)
50	5.7	6.8	5.8	4.4
100	7.6	3.7	3.3	2.4
150	9.1	1.9	2.0	1.23

Table 3.4: A summary of the Stable Large Eddy Simulation Wind Field Provided by the National Center for Atmospheric Research, with a Monin-Obukhov Stability Parameter of zi/L = 2

Transverse coherence curves for separations in the y and z directions for the u component derived from the LES wind field are shown in figure 3.11 for transverse separations of 1, 2, 4, 8, and 16m. This range of separations is typical of transverse distances used in the calculations in section 6. Coherence curves were measured in the y direction at a height of 100m and in the z direction at all heights, the coherence curves in the lower half of the wind field are used to calculate average coherence curves for heights between 50m and 100m. Likewise, the coherences in the upper half of the wind field are averaged to produce a single family of coherence curves for heights between 100m and 150m. Coherence in the z direction is much lower than in the y direction, likely due to stable stratification in the wind field. Because the coherence curves for the u, v, and w components are similar, the u component coherences are used to describe all three components in this report.

Because of wind shear, wind evolution as a function of the longitudinal separation between points varies with height. In general, as the mean streamwise wind speed increases, the coherence curves for a given longitudinal separation increase, because

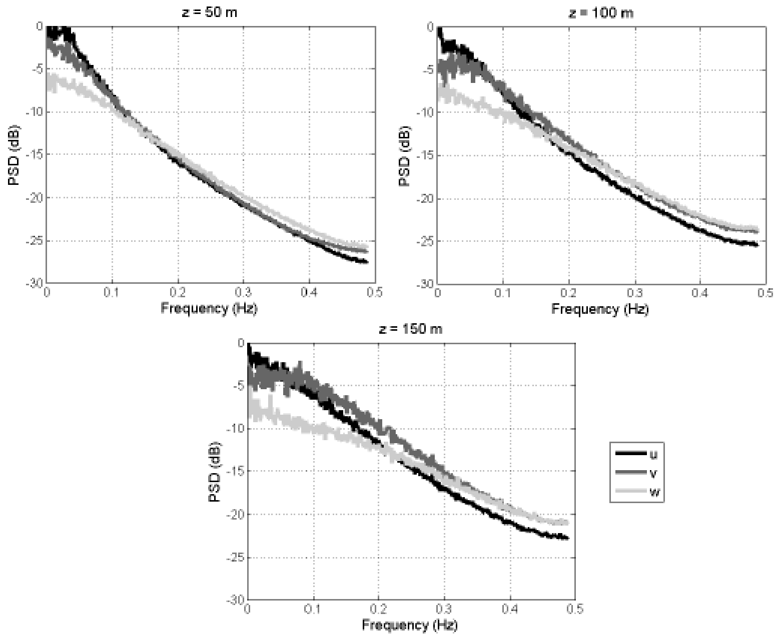

Figure 3.10: Power spectral densities of wind speed components at heights of 50m, 100m, and 150m for the stable large eddy simulation wind field described in Table 3.4.

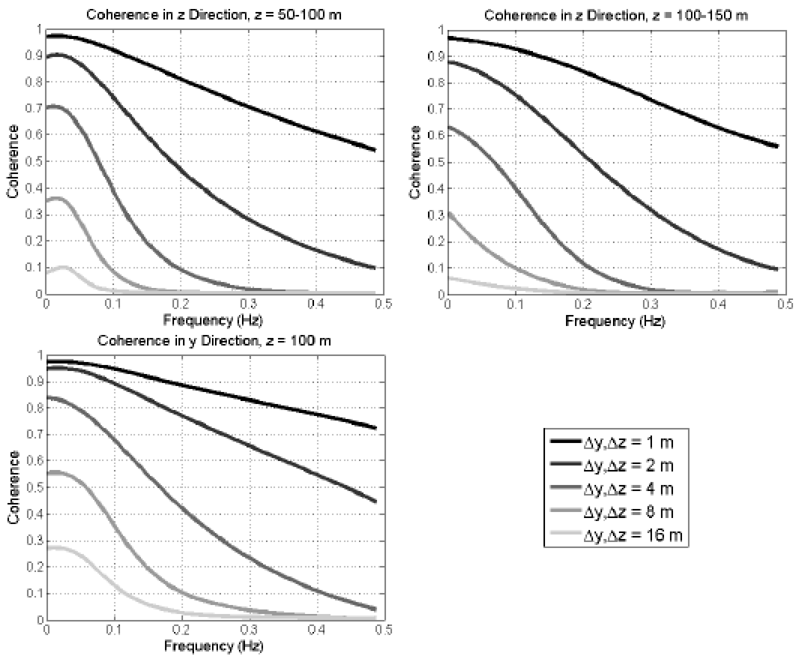

Figure 3.11: Transverse coherence curves for the stable LES wind field measured in the y direction at a height of 100m, and average coherence curves in the z direction based on measurements at heights between 50 and 100m and 150m.

the time that elapses as wind travels the same distance decreases. Figure 3.12 contains longitudinal coherence curves for the u component based on measurements at a height of 100m for longitudinal separations of 10, 25, 50, 100, and 200m. The measurement scenarios examined in section6 include preview distances up to 200m. Because of wind shear, coherence curves for heights above 100m are generally higher for a given frequency while curves for heights below 100m are lower. As a simplification, the coherence curves for the u components are determined at the height of 100m and are used to describe wind evolution for all components at all heights.

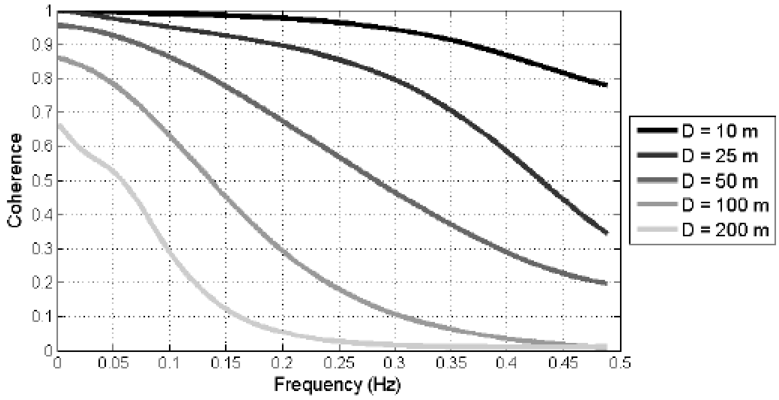

Figure 3.12: Longitudinal coherence curves for the stable LES wind field based on measurements at a height of 100m

CHAPTER 4

RESULTS AND DISCUSSIONS

4.1 Lidar Measurement Coherence

The quality of a wind speed measurement as influenced by evolution can be judged by the coherence between the estimate of the u component of the line-of-sight lidar system measurement and the true u component that reaches the rotor plane. Referring to figure 4.1, the upwind point at which the lidar is focused is called point

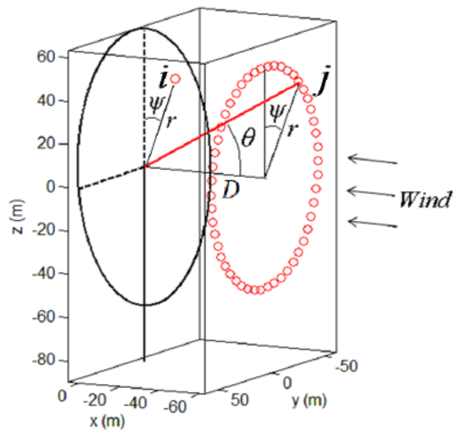

Figure 4.1: Coordinate system and measurement variables used. The lidar is assumed to mounted in the wind hub at $(x_h, y_h, z_h) = (0, 0, 0)$.

j, while the point where the evolved wind meets the rotor plane is called point i. Points i and j have the same transverse coordinates in the yz plane but are separated longitudinally by the preview distance D. The coherence between the estimate of the u component at point j and the true component at point i is written as (cf Eq. (2.35)):

$$\gamma^2_{u_i\hat{u}'_j}(f) = \frac{|S_{u_i\hat{u}'_j}(f)|^2}{S_{u_iu_i}(f)S_{\hat{u}'_j\hat{u}'_j}(f)} \tag{4.1}$$

where $\hat{u}'_j$ =the estimate of the u component based on the line-of-sight lidar measurement.

The following derivation of the measurement coherence yields a formula in terms of power spectral densities of the wind and coherence functions for any pair of points in the wind field, which are assumed as known quantities and are based on the wind field description in §§ 3.5. This derivation is based on an analysis given by Schlipf, for the simple case where there is neither range weighting nor wind evolution [50]. While measurement coherence can be estimated by simulating lidar measurements in an evolving wind field, the formulas to calculate measurement coherence is that direct calculations of coherence using spectral properties of the wind field are much less computationally expensive than time-domain simulations of lidar measurements. In addition, properties of the wind field can be easily varied without generating additional four-dimensional wind fields.

If the unit vector is represented in the direction that the lidar is pointing as $\boldsymbol{l} = [l_x, l_y, l_z]$ then, based on the coordinate system in figure 4.1, the line-of-sight wind speed measurement is

$$u_{j,\text{los}} = l_x u_j - l_y v_j - l_z w_j \tag{4.2}$$

Furthermore, the range weighted line-of-sight measurement is represented as;

$$u'_{j,\text{los}} = l_x u'_j - l_y v'_j - l_z w'_j \tag{4.3}$$

where the range weighted velocity vector is given by

$$\boldsymbol{u}'_j = \int_0^\infty \boldsymbol{u}(R\boldsymbol{l})W(F,R)dR \tag{4.4}$$

with $\boldsymbol{u} = [u, v, w]$.

Based on Eqs. (4.2) and (4.3), the estimate of the u component of a line-of-sight point measurement is given by

$$\begin{aligned} \hat{u}_j &= \frac{u_{j,\text{los}}}{l_x} \\ &= u_j - \frac{l_y}{l_x} v_j - \frac{l_z}{l_x} w_j \end{aligned} \tag{4.5}$$

and the estimate of u for a line-of-sight range weighted measurement is given by

$$\begin{aligned} \hat{u}'_j &= \frac{u'_{j,\text{los}}}{l_x} \\ &= u'_j - \frac{l_y}{l_x} v'_j - \frac{l_z}{l_x} w'_j \end{aligned} \tag{4.6}$$

Using Eqs. (4.2) through (4.6), the terms $S_{\hat{u}'_j \hat{u}'_j}(f)$ and $S_{u_i \hat{u}'_j}(f)$ from Eq. (4.1) can be written in terms of the transverse and longitudinal coherence functions in the wind field and the power spectral density functions of the wind speeds. Letting $\hat{U}(f) = F\{\hat{u}(t)\}$ and $\{\cdot\}^*$ represent the complex conjugate operation, the $S_{\hat{u}'_j\hat{u}'_j}(f)$ term can be expanded as:

$$
\begin{aligned}
S_{\hat{u}'_j\hat{u}'_j}(f) &= \overline{\hat{U}'_j(f)\hat{U}'^*_j(f)} \\
&= \overline{\left(\int_0^\infty W(F,\alpha)\hat{U}(\alpha\boldsymbol{l},f)d\alpha\right)\left(\int_0^\infty W(F,\beta)\hat{U}^*(\beta\boldsymbol{l},f)d\beta\right)} \\
&= \int_0^\infty \int_0^\infty W(F,\alpha)W(F,\beta)\,\overline{\hat{U}(\alpha\boldsymbol{l},f)\hat{U}^*(\beta\boldsymbol{l},f)}\,d\alpha d\beta \\
&= \int_0^\infty \int_0^\infty W(F,\alpha)W(F,\beta)\,S_{\hat{u}_{\alpha\boldsymbol{l}}\hat{u}_{\beta\boldsymbol{l}}}(f)\,d\alpha d\beta
\end{aligned} \tag{4.7}
$$

where $S_{\hat{u}_{\alpha\boldsymbol{l}}\hat{u}_{\beta\boldsymbol{l}}}(f) =$ the cross-power spectral density (CPSD) between the estimates of the u components at points with distances α and β along the lidar beam. For each α, β pair, $S_{\hat{u}_{\alpha\boldsymbol{l}}\hat{u}_{\beta\boldsymbol{l}}}(f)$ can be expanded as

$$
\begin{aligned}
S_{\hat{u}_{\alpha\boldsymbol{l}}\hat{u}_{\beta\boldsymbol{l}}}(f) &= \overline{\hat{U}_{\alpha\boldsymbol{l}}(f)\hat{U}^*_{\beta\boldsymbol{l}}(f)} \\
&= \overline{\left(U_{\alpha\boldsymbol{l}}(f) - \frac{l_y}{l_x}V_{\alpha\boldsymbol{l}}(f) - \frac{l_z}{l_x}W_{\alpha\boldsymbol{l}}(f)\right)\left(U^*_{\beta\boldsymbol{l}}(f) - \frac{l_y}{l_x}V^*_{\beta\boldsymbol{l}}(f) - \frac{l_z}{l_x}W^*_{\beta\boldsymbol{l}}(f)\right)} \\
&= S_{u_{\alpha\boldsymbol{l}}u_{\beta\boldsymbol{l}}}(f) + \left(\frac{l_y}{l_x}\right)^2 S_{v_{\alpha\boldsymbol{l}}v_{\beta\boldsymbol{l}}}(f) + \left(\frac{l_z}{l_x}\right)^2 S_{w_{\alpha\boldsymbol{l}}w_{\beta\boldsymbol{l}}}(f) \\
&\quad - \frac{l_y}{l_x}\left(S_{u_{\alpha\boldsymbol{l}}v_{\beta\boldsymbol{l}}}(f) + S_{v_{\alpha\boldsymbol{l}}u_{\beta\boldsymbol{l}}}(f)\right) - \frac{l_z}{l_x}\left(S_{u_{\alpha\boldsymbol{l}}w_{\beta\boldsymbol{l}}}(f) + S_{w_{\alpha\boldsymbol{l}}u_{\beta\boldsymbol{l}}}(f)\right) \\
&\quad + \frac{l_y l_z}{l_x^2}\left(S_{v_{\alpha\boldsymbol{l}}w_{\beta\boldsymbol{l}}}(f) + S_{w_{\alpha\boldsymbol{l}}v_{\beta\boldsymbol{l}}}(f)\right)
\end{aligned} \tag{4.8}
$$

The measurement scenarios discussed in this report include azimuth angles of $\psi = 0°$, $\psi = 90°$, $\psi = 180°$, and $\psi = -90°$. As a result, the unit vector in the lidar direction either contains $l_y = 0$ or $l_z = 0$. In this case, Eq. (4.8) simplifies to

$$
\begin{aligned}
S_{\hat{u}_{\alpha\boldsymbol{l}}\hat{u}_{\beta\boldsymbol{l}}}(f) &= S_{u_{\alpha\boldsymbol{l}}u_{\beta\boldsymbol{l}}}(f) + \left(\frac{l_y}{l_x}\right)^2 S_{v_{\alpha\boldsymbol{l}}v_{\beta\boldsymbol{l}}}(f) + \left(\frac{l_z}{l_x}\right)^2 S_{w_{\alpha\boldsymbol{l}}w_{\beta\boldsymbol{l}}}(f) \\
&\quad - \frac{l_y}{l_x}\left(S_{u_{\alpha\boldsymbol{l}}v_{\beta\boldsymbol{l}}}(f) + S_{v_{\alpha\boldsymbol{l}}u_{\beta\boldsymbol{l}}}(f)\right) - \frac{l_z}{l_x}\left(S_{u_{\alpha\boldsymbol{l}}w_{\beta\boldsymbol{l}}}(f) + S_{w_{\alpha\boldsymbol{l}}u_{\beta\boldsymbol{l}}}(f)\right)
\end{aligned} \tag{4.9}
$$

The complex-valued CPSD in Eq. (4.9) can be written in terms of its magnitude and phase as

$$
S_{\hat{u}_{\alpha\boldsymbol{l}}\hat{u}_{\beta\boldsymbol{l}}}(f) = \left|S_{\hat{u}_{\alpha\boldsymbol{l}}\hat{u}_{\beta\boldsymbol{l}}}(f)\right| e^{i\varphi_{\alpha\boldsymbol{l}\beta\boldsymbol{l}}(f)} \tag{4.10}
$$

Each term in Eq. (4.9) has the same phase, which is given by:

$$
\varphi_{\alpha\boldsymbol{l}\beta\boldsymbol{l}}(f) = \frac{D_{\alpha\boldsymbol{l}\beta\boldsymbol{l}}(f)}{\bar{U}} \tag{4.11}
$$

where $D_{\alpha l \beta l}$ is the longitudinal separation between points at distances α and β along the lidar beam.

The calculation of the $S_{u_i \hat{u}'_j}(f)$ term from Eq. (4.1) is performed in a similar fashion as the $S_{\hat{u}'_j \hat{u}'_j}(f)$ term.

4.2 Components of Measurement Coherence

There are several factors that may cause a decrease in measurement coherence as defined by Eq. (4.1). In addition to wind evolution, error sources that are characteristics of lidar measurements in non-evolving wind fields, such as range weighting and directional bias, will cause a loss of coherence. Figure 4.2 and 4.3 compare the components of coherence for three different measurement geometries by showing the measurement coherence that was calculated using Eqs. (4.1) through (4.11) with various combination of the error sources included. Figure 4.2 uses the spectral properties of the TurbSim wind field with exponential wind evolution, while figure 4.3 uses characteristics of the large eddy simulation (LES) wind field. The decay parameter used with the exponential model is $a = 0.45$. Coherence plots for both wind fields are provided to compare and contrast the simple wind evolution model and the model that is derived from the LES results. In both figures, each scenario involves a lidar that is located at the hub, measuring wind at a radial distance of $r = 47.25$m at an azimuth angle of $\psi = 90°$, but with different preview distances ($D = 24$, 58, and 130m). The curves in figure 4.2 and 4.3 do not include the effects of uv or uw correlation in order to highlight the other sources of coherence loss. Although the exact measurement curves differ for the two wind field models, the following trends apply to both scenarios. When $D = 24$m, the measurement angle is large, longitudinal coherence (dashed) is relatively high, and the effects of range weighting are insignificant due to the short focal distance. Here, directional bias dominates the overall coherence, with wind evolution causing some degradation at higher frequencies. When $D = 130$m, the measurement angle is low, longitudinal coherence is low, due to wind evolution, and range weighting is significant due to the long focal distance. Wind evolution, is the dominant component of measurement coherence, with range weighting adding a further loss of coherence. For the $D = 58$m scenario, all three sources of coherence loss are significant. Directional bias and wind evolution, both have very strong impacts, with range weighting causing an additional loss of coherence.

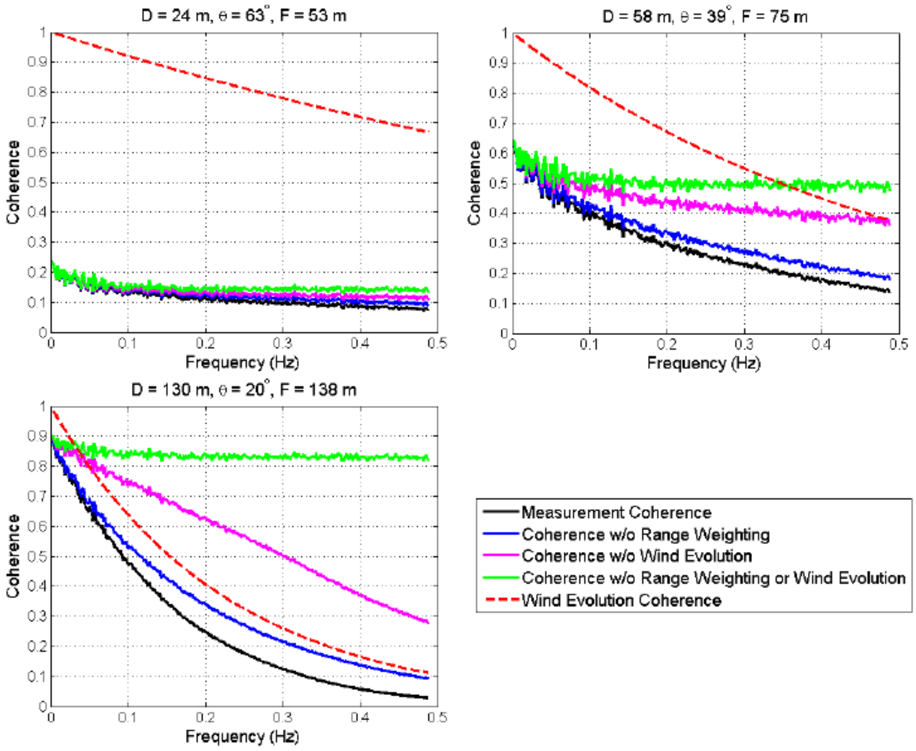

Figure 4.2: A comparison of the components of measurement of coherence for a scanning LIDAR scenario, with scan radius $r = 47.25$m using the Great Plains-Low Level Jet wind field and exponential coherence with $a = 0.45$

Figure 4.2 and 4.3 reveal that the (green) coherence curves from directional bias alone are relatively constant over all frequencies and increase as the measurement angle decreases. Although not shown in figure 4.2 or 4.3, when the effects of uv and uw coherence (present in the Great Plains-Low Level Jet wind field) are included, measurement coherence, due to directional bias, changes because of the non-zero correlation between the u and v as well as u and w components. By comparing the green and magenta curves, it can be seen that range weighting adds a significant coherence loss when wind evolution is not included, especially for larger preview distances. However, by comparing the blue and black curves, it is clear that with wind evolution included, range weighting never dominates the overall coherence loss.

4.3 Lidar Measurements of Evolving Wind Fields

Two metrics are used to reveal the measurement quality for different scan geometries. The first metric is the "coherence bandwidth," defined here as the bandwidth where

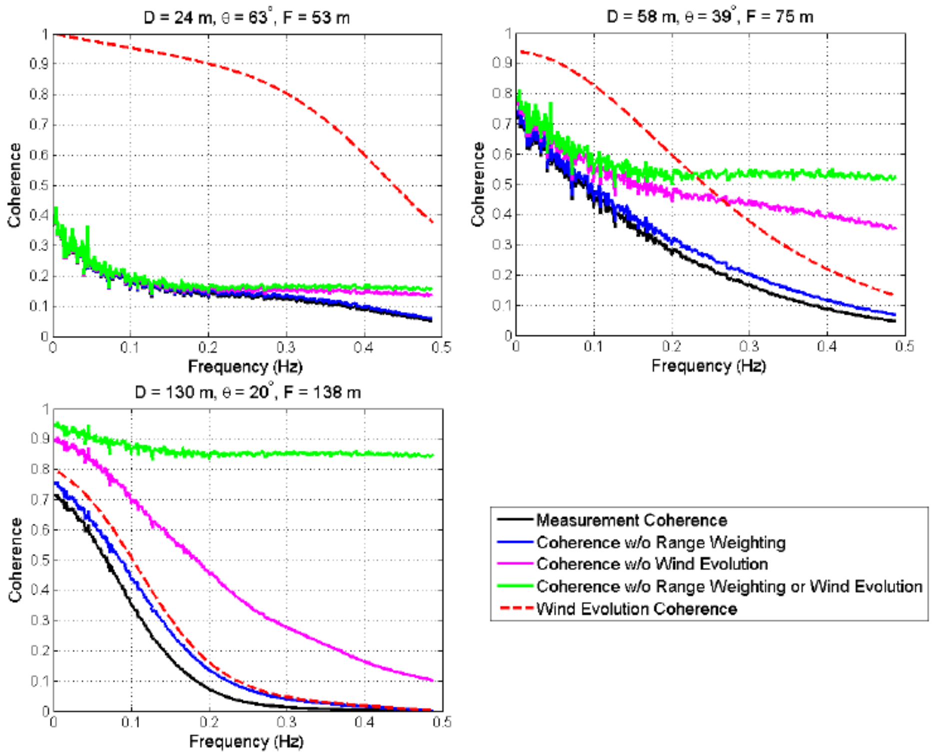

Figure 4.3: A comparison of the components of measurement of coherence for a scanning LIDAR scenario, with $r = 47.25$m using the stable Large Eddy Simulation (LES) wind field and evolution model

the measurement coherence remains above 0.5. A higher coherence bandwidth yields a better measurement, because more of the measured turbulence spectrum can be used in a wind preview-based controller. The second metric is the integral of measurement coherence, or the area under the coherence curve. The integration is only performed for a bandwidth of about 0.5 hertz (HZ), based on the Nyquist frequency of the LES wind field. A larger area under the coherence curve will yield a better measurement. Results based on the two metrics are similar, but both are provided here for comparison.

The following results compare measurement quality for different scan geometries and reveal the optimal preview distances in terms of maximising the coherence bandwidth or coherence integration. For the exponential wind evolution model, the decay parameter a is varied to show the impact that wind evolution intensity has on optimal preview distance. For the LES-based model, the results reveal what typical preview distances might be in a stable wind field with physics-based wind evolution, but a wind field that is less productive from a wind energy perspective.

Separate results are provided for four different lidar azimuth angles ($\psi = 0°$, $90°$, $180°$, $-90°$) because the wind spectra and transverse coherences vary with height and direction. In addition, for the TurbSim generated wind field, the uv and uw correlations will have different impacts on measurement coherence (depending on azimuth angle).

The chosen scan geometries are based on the National Renewable Energy Laboratory (NREL) 5-megawatt (MW) turbine model. Scan radii of 15.75m, 31.5m, 47.25m, and 63m are investigated, which corresponds to 25%, 50%, 75%, and 100% blade span. For the Great Plains-Low Level Jet scenario, the lidar is located at a height of 90m, but for the LES wind field, the lidar is located at a height of 100m, which is the center of that wind field.

4.4 Measurements Using the Exponential Wind Evolution Model

For the TurbSim wind field with the exponential wind evolution model, results are provided for $\psi = 90°$and $\psi = -90°$, where the lidar is only measuring wind in the xy plane, $\psi = 0°$, where the lidar is measuring wind in the xz plane above hub height, and $\psi = 180°$, where wind is measured in the xz plane below hub height. These four azimuth angles were chosen because the wind spectra and transverse coherences are different in the y and z directions. In addition, l_y will be positive for $\psi = 90°$and negative for $\psi = -90°$. Similarly, l_z will be positive for $\psi = 0°$and negative for $\psi = 180°$. Furthermore, the spectra and transverse coherence curves vary with height, so measurements above and below hub height are analysed.

Figure 4.4 compares the $\gamma^2 = 0.5$ coherence bandwidths of measurement coherence as a function of preview distance for a range of decay parameters. Note that the green curves represent a decay parameter $a = 0$, which is equivalent to no wind evolution (Taylor's frozen turbulence hypothesis). Coherence bandwidth curves are provided for the four different azimuth angles. For shorter scan radii, the preview distances that provide maximum coherence bandwidth are shorter, because the degradation caused by directional bias that enters the coherence calculations through Eq. (4.9) is lower than for larger scan radii. Therefore, with small scan radii, the dominant source of coherence loss transitions from directional bias to wind evolution or range weighting at shorter preview distances.

In figure 4.4, the curves for azimuth angles $\psi = 90°$and $\psi = 180°$are very similar,

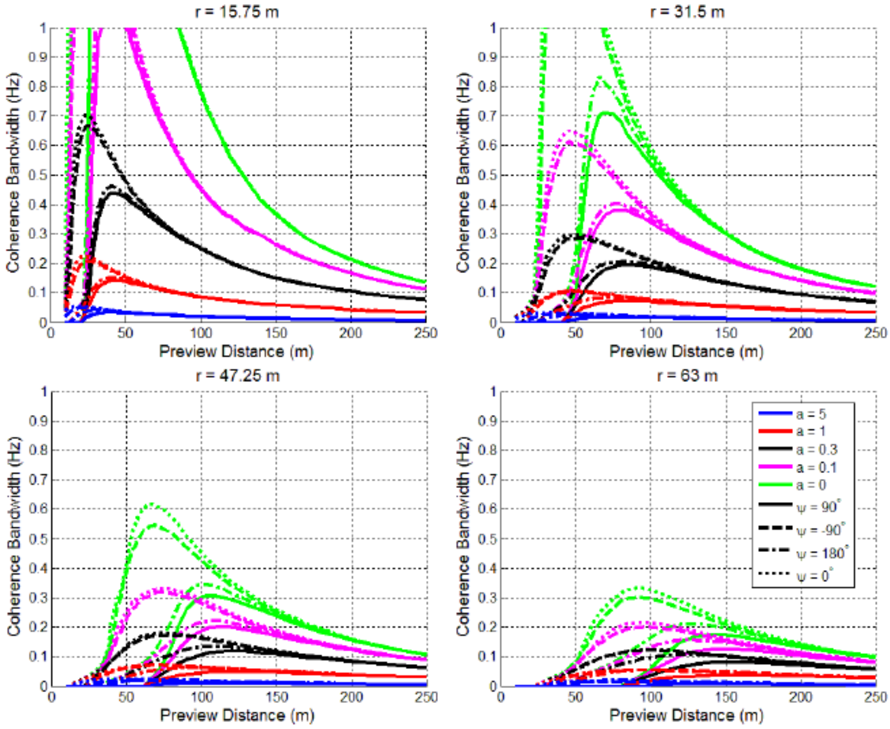

Figure 4.4: This figure shows the $\gamma^2 = 0.5$ coherence bandwidth versus preview distance for the Great Plains-Low Level Jet wind field for scan radii of $r = 15.75$, 31.5m, 47.25m and 63m. The wind evolution is based on an exponential coherence model with various decay parameters.

as are the curves for azimuth angles $\psi = 0°$and $\psi = -90°$. For $\psi = 90°$and $\psi = 180°$, the cross-power spectral densities (CPSDs), between the u and v as well as the u and w components, introduce a negative contribution in Eq. (4.9) and the similar expression for the $S_{u_i\hat{u}'_j}(f)$ term. This behaviour is due to l_y and $S_{uv}(f)$ both having positive signs and l_z and $S_{uw}(f)$ both having negative signs. The negative contribution of the v and w components causes a reduction in both the magnitude of the measured lidar signal and the overall measurement coherence. In contrast, for $\psi = -90°$and $\psi = 0°$, l_y is negative while the sign of $S_{uv}(f)$ is positive, and l_z is positive while the sign of $S_{uw}(f)$ is negative. Therefore, the CPSDs, between the u and v as well as the u and w components, introduce a positive contribution in Eq. (4.9) and the similar expression for the $S_{u_i\hat{u}'_j}(f)$ term. The positive contribution of the v and w components causes an increase in both the magnitude of the measured lidar signal and the overall measurement coherence.

Although the influence of the uv and uw cross-correlations is the main factor contributing to the azimuthal dependence of measurement coherence, further variations between the curves for different azimuth angles in figure 4.4 reveal how the relative magnitudes of the wind spectra components affect measurement coherence. Measurements at an azimuth angle of $\psi = 0°$in the xz plane produce slightly higher coherence bandwidths than measurements at $\psi = -90°$in the xy plane. Likewise, measurements at an azimuth angle of $\psi = 180°$in the xz plane produce higher coherence bandwidths than measurements at $\psi = 90°$in the xy plane. The improved results for the measurements in the xz plane can be explained by examining the wind spectra in figure 3.8. The ratio between the v component of the wind spectrum and the u component is greater than the ratio between the w and u components at all heights, so the v component of the wind corrupts measurements more than the w component. Therefore, when measurements are confined to the xy plane, there is more coherence loss due to directional bias effects than when measurements are confined to the xz plane.

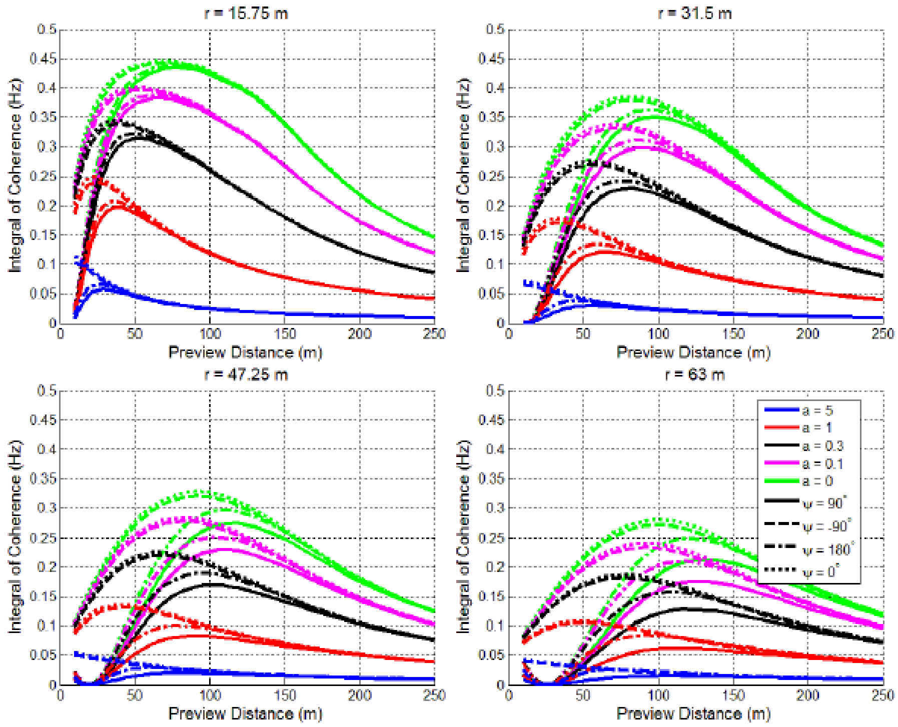

Figure 4.5: Integral of measurement coherence from 0Hz to 0.5Hz versus preview distance for the Great Plains-Low Level Jet wind field for scan radii of $r = 15.75$m, 31.5m,47.25m and 63m. Wind evolution is based on an exponential coherence model with various decay parameters.

Figure 4.5 shows results for the same measurement scenarios as in figure 4.4, but with the integral of the coherence curves as the measurement quality metric. Most of the trends are similar to those in figure 4.4, but with slightly different optimal preview distances.

While the maximum coherence bandwidths are much lower for larger decay parameters, as can be expected, interestingly, the optimal measurement preview distances do not change very much as a is varied when using the coherence bandwidth metric. When using the integral of coherence as a metric, the optimal preview distance is much more sensitive to changes in the decay parameter.

CHAPTER 5

CONCLUSIONS

5.1 Summary

In this thesis, lidar simulation results show that for a circular scan pattern, a scan radius close to 70% rotor radius provides the strongest measurement correlation. Small scan radii, such as $r = 0.1R$ produce lower correlations because the measured winds are representative of a smaller portion of the rotor plane. For preview distances roughly equivalent to the rotor radius, the coherence drops as the preview distance increases due to wind evolution. However, preview distance must roughly double before coherence drops by more than 0.1. When knowledge of the wind speed and direction at heights other than hub height is used to determine the scan geometry, measurement coherence can be increased, but at most by 0.1 for $r = 0.7R$ and $24\text{m} < D < 130\text{m}$.

The modified scan pattern (temporal attenuation) improves measurement quality more for longer preview distances. The general scan pattern optimization results show that: (i) as the number of beams increases, the measurement accuracy increases as well and (ii) additional measurement ranges afforded by pulsed lidars improve measurement accuracy.

Coherence bandwidth is maximized using shorter preview distances which prevent the coherence at higher frequencies from decaying too much from wind evolution. Measuring the wind farther away than the optimal preview distances causes wind evolution to become more severe, increasing measurement error as well. The extra preview time provided by longer preview distances are useful when attempting to detect extreme wind events and take necessary action to protect the turbine. However, using coherence bandwidth as a metric, it was revealed that, for a given scan radius, the optimal preview distance is not very sensitive to the amount of wind evolution. Optimal preview distances based on the coherence bandwidth for lidar measurements in the unstable Great plains wind field, are roughly 60m for a scan radius of $r = 31.5\text{m}$, 80m for $r = 47.25\text{m}$, and 120m for $r = 63\text{m}$ for decay parameters less than one. These approximate optimal preview distances are formed by averaging over all four azimuth angles.

Measuring the wind at multiple range gates with pulsed lidar offers the advantage of being able to track wind speeds as they travel towards the turbine as well as allowing measurements at different preview distances to be combined to improve the simultaneous estimation of wind shear and direction. Thus from a controls perspective, a preview measurement at 47.25m or 75% rotor radius for the 5 MW model is the most useful due to maximum power capture near this blade span. The results reveal that the bandwidth of coherent measurements at $r = 47.25$m is roughly 0.11Hz based on $\gamma^2 = 0.5$ bandwidth definition.

When comparing results based on coherence bandwidth for different decay parameters, it can be seen that unless the intensity of evolution is very strong, the optimal preview distances are almost the same with wind evolution or without ($a = 0$). Using the integral of coherence as a metric, the optimal preview distances vary considerably as the decay parameter changes.

5.2 Perspectives (Future Outlook)

- Future research might need to explore boundary layers that are unstable. That is, establishing how wind evolution varies with the atmospheric stability.
- There are many promising direction that lidars for control applications could take in the future:
  - The design of Lidar-Assisted Control (LAC) scenarios for extreme event detection is gaining importance.
  - New approaches to wind field estimation, such as coupling of raw lidar measurements with fluid dynamic models, are being explored.
- The effect of induction zone upwind of the rotor. This extends roughly one rotor diameter in front of the turbine, and has the effect of slowing down the advection velocity of the wind near the rotor, thereby detecting the streamlines around the rotor disc by some amount and distorting the turbulence. The impact of the induction zone on wind speed measurements is an area of future study.

BIBLIOGRAPHY

[1] Eric Simley, Holger Fürst, Florian Haizmann and David Schlipf, "Optimizing Lidars for Wind Turbine Control Applications—Results from the IEA Wind Task 32 Workshop" *Remote Sens.* **2018**, *10, 863.*

[2] Andrew Scholbrock, Paul Fleming, David Schlipf, Alan Wright, Kathryn Johnson and Na Wang, "Lidar-Enhanced Wind Turbine Control: Past, Present and Future", *National Renewable Energy Laboratory, NREL/CP-5000-65879*, **2016**.

[3] T. Mikkelsen, "Lidar-based research and innovation at DTU Wind Energy – a review," *Journal of Physics: Conference Series,* vol.**524**, no. **1**, **2014**.

[4] P. Towers and B. LI. Jones, "Real-time wind field reconstruction from LiDAR measurements using a dynamic wind model and state estimation" *Wind Energ.* ***(2014)*** *DOI: 10.1002/we.1824.*

[5] Lindenberg, S., Smith, B., and O'Dell, K., 20% wind energy by 2030. **2008**. National Renewable Energy Laboratory (NREL), US Department of Energy, Renewable Energy Consulting Services, Energetics Incorporated, United States.

[6] Abdel Ghani Aissaoui and Ahmed Tahour, Wind Turbines: Design, Control and Applications, Published by ExLi4EvA, Copyright© **2016**, www.Ebook777.com

[7] Funke (2017-06-09). "MHI Vestas launched the world's most powerful wind turbine". *Offshore Wind Industry.* Retrieved 2018-01-24.

[8] D. Schlipf, J. Mann, and P.W. Cheng, "Model of the correlation between lidar systems and wind turbines for lidar assisted control," *Journal of Atmospheric and Oceanic Technology*, vol.**30**, no.**10**, **pp.** 2233-2240, **2013**.

[9] D. Schlipf, S. Kapp, J. Anger, O. Bischoff, M. Hofs, A. Rettenmeier, and M. Kühn, "Prospects of optimization of energy production by lidar assisted control of wind turbines," in EWEA *2011 conference proceedings*, Brussels, Belgium, **2011**.

[10] Luis Arturo Soriano, Wen Yu, Jose de Jesus Rubio. "Modeling and Control of Wind Turbine" in *Mathematical Problems in Engineering* (**2013**). *DOI: 10.1155/2013/982597.*

[11] David Schlipf, et al. "Detection of Wind Evolution and Lidar Trajectory Optimization for Lidar-Assisted Wind Turbine Control." January **2015**. *DOI: 10.18419/opus-8417*.

[12] Betz, A.: Windenergie und ihre Ausnutzung durch Windmühlen,Vandenhoek und Rupprecht 1926; Viewag, Göttingen 1946

[13] David Schlipf, Dominik Johannes Schlipf and Martin Kühn, "Nonlinear model predictive control of wind turbines using LIDAR" *Wind Energ.* **(2012)** *DOI: 10.1002/we.1533*.

[14] Cracknell, Arthur P.; Hayes, Ladson (2007) [1991]. Introduction to Remote Sensing (2 ed.). London: Taylor and Francis. **ISBN** 978-0-8493-9255-9. OCLC 70765252.

[15] C. Weitkamp, Lidar: Range-Resolved Optical Remote Sensing of the Atmosphere, ser. Springer series in Optical Sciences. Springer, 2005.

[16] A. Jelalian, Laser Radar Systems, ser. Artec House Radar Library. Artec House, Incorporated, 1992.

[17] Philosophical Magazine and Journal of Science, 1930, Series 7, Volume 9, Issue 60, pp. 1014–1020.

[18] Donegan, J.F.; The Life and Works of Edward Hutchinson Synge pp. 31, 67, (co-edited with D. Weaire and P. Florides), Pöllauberg, Austria : Living Edition, ISBN 3901585176

[19] 'Experimental Advanced Airbone Research Lidar', USGS.gov. Retrieved 8 August 2007.

[20] Amzajerdian, Farzin; Pierrottet, Diego F.; Petway, Larry B.; Hines, Glenn D.; Roback, Vincent E. (2011-05-24). "Lidar Systems for Precision Navigation and Safe Landing on Planetary Bodies". International Symposium on Photoelectronic Detection and Imaging 2011: Laser Sensing and Imaging; and Biological and Medical Applications of Photonics Sensing and Imaging. 8192: 819202. Bibcode:2011SPIE.8192..02A doi:10.1117/12.904062 hdl:2060/20110012163. Retrieved May 24, 2011.

[21] Rashid A. Ganeev. Laser-Surface Interactions. Springer Science & Business Media, 2013. p. 32.

[22] J. P. Cariou, "Pulsed lidars," in *Remote Sensing for Wind Energy, DTU Wind Energy-E-Report-0029(EN)*, June 2013, ch. 5, pp. 104-121.

[23] M. Pitter, C. Slinger, and M. Harris, "Introduction to continuous-wave doppler lidar," in *Remote Sensing for Wind Energy, DTU Wind Energy-E-Report-0029(EN)*, June 2013, ch. 4, pp. 72-103.

[24] R. S. Hansen and C. Pedersen, "All semiconductor laser Doppler anemometer at 1.55μm," *Opt. Express*, vol. 16, no. 22, p. 18288, 2008.

[25] P. J. Rodrigo and C. Pedersen, "Field performance of an all-semiconductor laser coherent Doppler lidar," *Opt. Lett.*, vol. 37, no. 12, p. 2277, 2012.

[26] Martion O. L. Hansen. Aerodynamics of Wind Turbines. 2nd ed. ISBN: 978-1-84407-438-9. Earthscan, London Sterling, VA. 2008

[27] Panofsky, H. (1974). The atmospheric boundary layer below 150 metres. *Annual Review of Fluid Mechanics* **6**, 147–177.

[28] Freris, L., editor (1990). *Wind Energy Conversion Systems.* Prentice Hall, Hertforshire, UK.

[29] Walker, J. and Jenkins, N. (1997). *Wind Energy Technology.* John Wiley & Sons, Chichester, UK.

[30] Johann Friedrich Gülich (2010). *Centrifugal Pumps (2nd ed.).* Berlin: Springer-Verlag. ISBN 978-3-642-12823-3.

[31] Stull RB. *An Introduction to Boundary Layer Meteorology*, Vol. 13. Springer: New York City, 1988.

[32] M. Born and J.R. Oppenheimer, Ann. Phys. 87, 457 (1927).

[33] D. F. Swinehart. J. Chem. Educ. 1962, 39, 7, 333. July 1, 1962

[34] Jonathan Mitschele. J. Chem. Educ. 1996, 73, 11, A260. November 1, 1996

[35] Collis, R. T. H. (1966) "Lidar: a New Atmospheric Probe," *Q. J. R. Meteorol. Soc.*, **92**, 220–230.

[36] F. G. Fernald: Appl. Opt. **23**, 652 (1984)

[37] J. D. Klett: Appl. Opt. 20, 211 (1981)

[38] F.G. Fernald, B.M. Herman, J.A. Reagan: J. Appl. Meteorol. 11, 482 (1972)

[39] Y. Sasano, E.V. Browell, S. Ismail: Appl. Opt. 24, 3929 (1985)

[40] D. Schlipf, S. Kapp, J. Anger, O. Bischoff, M. Hofsäß, A. Rettenmeier, U. Smolka, and M. Kühn, "Prospects of optimization of energy production by LiDAR assisted control of wind turbines," in *Proceedings of the European Wind Energy Association annual event*, Brussels, Belgium, 2011.

[41] D. Schlipf, A. Rettenmeier, F. Haizmann, M. Hofsäß, M. Courtney, and P. W. Cheng, "Model based wind vector field reconstruction from lidar data," in *Proceedings of the German Wind Energy Conference DEWEK*, Bremen, Germany, 2012.

[42] Boquet M., Parmentier R. and Cariou J. P. (2009) Analysis and optimization of pulsed Doppler lidar in complex terrain. EWEC, Marseille

[43] Boquet M., Parmentier R. and Cariou J. P. (2010) Correction of pulsed wind lidars bias in complex terrain. ISARS

[44] Jonkman B. "TurbSim User's Guide: Version 1.50," NREL/TP-500-46198, Golden, CO: National Renewable Energy Laboratory, 2009.

[45] Dunne, F.; Pai, L.-Y.; Wright A.D.; Jonkman, B.; Kelley, N.; Simley, E. "Adding Feedforward Blade Pitch Control for Load Mitigation in Wind Turbines: Noncausal Series Expansion, Preview Control, and Optimized FIR Filter Methods," in *Proc. 49th AIAA Aerospace Sciences Meeting*, Orlando, FL, January 2011.

[46] Simley, E.; Pao, L.-Y.; Frehlich, R.; Jonkman, B.; Kelley, N. "Analysis of Wind Speed Measurements Using Coherent LIDAR for Wind Preview Control," in *Proc. 49th AIAA Aerospace Sciences Meeting*, Orlando, FL, January 2011.

[47] Dunne, F.; Pao, L.; Wright, A.; Jonkman, B.; Kelley, N. "Combining Standard Feedback Controllers with Feedforward Blade Pitch Control for Load Mitigation in Wind Turbines," in *Proc. 48th AIAA Aerospace Sciences Meeting*, Orlando, FL, January 2010.

[48] Pielke, R.A.; Panofsky, H.A. "Turbulence Characteristics along Several Towers," *Boundary Layer Meteorology*, Vol. 1, No. 2, 1970, pp. 115-130.

[49] Beare, B.; MacVean, M.; Holstag, A.; Cuxart, J.; Esau, I.; Golaz, J.; Jimenez, M.; Khairoutdinov, M.; Kosovic, B.; Lewellen, D.; Lund, T.; Lundquist, J.; McCabe, A.; Moene, A.; Noh, Y.; Raasch, S.; Sullivan, P. "An Intercomparison of Large-Eddy Simulations of the Stable Boundary Layer," *Boundary Layer Meteorology*, Vol. 118, No. 2, Dec. 2006, pp. 247–272.

[50] Schlipf, D. "Wind Turbine Control Using Lidar: Notes to Presentation," in *PhD Summer School: Remote Sensing for Wind Energy*, Roskilde, Denmark, June 2011.